Division of Biomedical Engineering
Department of Human Biology
University of Cape Town

Development of a Prospectively Motion Corrected Free-breathing FLASH Sequence.

Dissertation

In fulfillment of the requirements for the degree:
MSc. in Biomedical Engineering

Graeme Harris
HRRGRA004

Supervisor:
Prof. Ernesta Meintjes

Co-supervisor:
Mr. Stephen Jermy

April 7, 2023

Plagiarism Declaration

I know that plagiarism is wrong. Plagiarism is to use another's work and pretend that it is one's own.

I have used the **APA** convention for citation and referencing. Each contribution to, and quotation in, this dissertation from the work(s) of other people has been attributed and has been cited and referenced.

This dissertation is my own work.

I have not allowed, and will not allow, anyone to copy my work with the intention of passing it off as his or her own work.

Signed by candidate

April 7, 2023

Acknowledgements

Thank you deeply to my supervisors, Prof. Ernesta Meintjes and Mr. Stephen Jermy. You have guided everything from the basic implementation and structure of the research to aiding me in the writing of this dissertation. Thank you also to all those who volunteered to be scanned for this project and read through the many drafts. I would not have been able to complete this without you.

Abstract

Respiratory motion of the heart is a fundamental challenge to cardiac MR imaging (CMR). This motion is frequently compensated for with breath-holding and acceptance-window methods. In situations where breath-holding is not viable, navigated free-breathing with an acceptance window can be used. This method results in inefficient acquisitions, creating longer scan times. This dissertation outlines the implementation of an adaptive predictor-observer control system in a FLASH sequence.

The control system predicts the position of the diaphragm throughout the imaging segments based on multiple diaphragm position measurements acquired during the non-imaging segments. The position of the imaging slice is then prospectively adjusted using a linear scaling factor to perform slice following of the heart. Typically, a generalized scaling factor of 0.6 is used but this does not compensate for the variation amongst subjects nor the 3D nature of the heart.

The performance of the control system was tested on phantoms and in 8 healthy volunteers. All imaging was performed on a 3T Skyra (Siemens AG, Erlangen). Initial phantom testing was performed utilizing a motion rig that simulates tidal breathing motion. Five sets of ECG-triggered FLASH acquisitions were performed in each healthy volunteer: (i) breath-holds (BH), (ii) free-breathing with no motion correction, (iii) free-breathing navigated-FLASH with a 4mm acceptance window (gated), (iv) free-breathing navigated-FLASH adapted to utilize the control system, and (v) a set of low-resolution cine FLASH images (TR=86ms, 50 images). The log data from the acquisitions with the control system adapted sequence were then analysed to measure the accuracy of the control system's predictions. Images acquired with the standard BH sequence were compared to those from the control system adapted sequence, the acceptance window sequence, and the uncorrected free-breathing sequence. Finally, the set of cine images were segmented at the lung-liver interface and around the heart. The edge of the lung-liver interface and an edge of the heart were tracked to calculate the proportional change of the diaphragm's position to the heart's position, for each subject.

The error between the control system's predicted position of the diaphragm and estimated actual position was within the 4mm acceptance window used by the gated sequence. The root mean squared error (RMSE) was below 3mm for many of the acquisitions and below 4mm for all except three acquisitions. The resultant images show improved quality using the control system compared with no correction and similar quality when compared to the gated acquisition, although artifacts due to the expansion and contraction of the chest wall remained. Tracking the edge of the lung-liver interface and the heart yielded variable tracking factors across subjects (0.58 to 1.02).

Although the slice following of the control system is accurate, tracking during non-linear sections of the breathing cycle remains challenging. There remains a risk of large tracking inaccuracy if errors in median calculation occur. The linear tracking factors relating diaphragm positions to the heart positions are constant for each subject but vary greatly between each subject, indicating the need for further research into subject specific tracking factors for each individual acquisition. The control system adapted acquisition can provide similar image quality to the gated acquisition, for certain tracking factors, whilst maintaining 100% imaging efficiency through the respiratory cycle.

Contents

List of Figures

List of Tables

List of Terms

BRISQUE	Blind/Referenceless Image Spatial Quality Estimator
BH	Breath Held
CMR	Cardiac Magnetic Resonance
CT	Computed Tomography
CVD	Cardio-vascular Disease
ECG	Electrocardiogram
FB	Free Breathing
FFT	Fast Fourier Transform
FLASH	Fast Low Angle Shot
KCF	Kernelized Correlation Filter
MIL	Multiple Instance Learning
MIQA	Medical Image Quality Assessment
MRI	Magnetic Resonance Imaging
NEMA	National Electrical Manufacturers Association
PET	Positron Emission Tomography
PSNR	Peak Signal to Noise Ratio
RMSE	Root Mean Squared Error
ROI	Region of Interest

1 Introduction

1.1 Background of Study

Cardiovascular diseases (CVDs) are a group of disorders of the heart or blood vessels. The majority of CVDs globally are caused by non-communicable conditions and are therefore commonly grouped into the category of non-communicable diseases (NCDs). NCDs are responsible for the highest percentage of global mortality (73.4% of all deaths), with deaths due to CVD comprising the majority (Roth et al., 2018). Within South Africa, mortality due to CVD is second only to HIV/AIDS, and results in 17.3% of all deaths as of 2015. Furthermore, non-communicable diseases result in the highest percentage of total mortality in South Africa and this percentage has continued to rise from 2008 to 2016 (Maluleke, 2016).

Modern diagnosis of CVD is aided by non-invasive medical imaging. The most prevalent imaging modalities are positron emission tomography (PET), X-ray computed tomography (CT), ultrasound and magnetic resonance imaging (MRI). Of these modalities, MRI is able to accurately discern soft tissues, without exposure to ionizing radiation. However, MRI is a relatively slow process when compared with other imaging modalities. The long imaging acquisition time for MRI results in the process being highly sensitive to natural motions of the patient. These motions such as adjusting one's position for comfort, motion due to the beating heart and respiration can all result in ghosting artifacts in the final image, if not properly compensated for. The ghosting artifacts appear as faded repetitions of structures in the final image and therefore hamper the image's diagnostic utility.

While motion resulting from the beating heart is successfully compensated for by synchronising the MR acquisition to the cardiac cycle, respiratory motion still poses a challenge. An early and still widely used method for reducing errors due to respiratory motion requires patients to hold their breath during the acquisition. Breath-holds (10-20 seconds) are, however, difficult for patients to maintain and repeat reliably after fatigue sets in. It is therefore desirable to reduce the need for breath-holds during cardiac MRI.

1.2 Purpose of Study

This study aims to implement a slice following technique that updates the slice position multiple times throughout the imaging segment of an acquisition in order to compensate for respiratory motion. The slice position is updated by predicting the patient's diaphragm position throughout the cardiac cycle using a predictor observer control system first proposed by Burger (2012).

The control system navigated method will be implemented in the widely used Fast Low-Angle Shot (FLASH) sequence (Haase et al., 1986), thereby facilitating improved image quality during free-breathing cardiac MRI acquisition without any time penalty.

1.3 Scope and Limitations

The aim of this research was to integrate a previously developed predictive control system with the Siemens spoiled gradient FLASH MR sequence. The control system navigated sequence will be developed on the 3T Siemens MAGNETOM Skyra (Erlangen, Germany) MRI scanner located at the Cape Universities Body Imaging Centre (CUBIC).

The research proposed sought to meet the following objectives:

- Implement the predictive respiratory motion control algorithm within the FLASH MRI sequence.
- Investigate the effectiveness of the initial implementation when compensating for periodic breathing-like motion in a phantom.
- Compare the performance, in healthy volunteers, of the control system corrected FLASH sequence to that of standard breath-hold and navigator-gated techniques.

1.4 Outline of Thesis

Chapter 2 provides an overview of cardiac pathologies relevant to cardiac MRI. Alongside this, an explanation of spoiled gradient echo MR imaging is provided, which is commonly used for cardiac MR. The Siemens implementation of this sequence is known as the Fast Low-Angle Shot (FLASH) sequence, and forms the primary MR sequence explored in this study. The challenges of motion correction in cardiac MR imaging are then outlined, with various existing correction techniques explored. This study implements a predictor-observer controller as a method of motion correction. The details of this controller are explained and the importance of subject specific parameters are outlined. In Section 3, the adaption of the FLASH sequence is then tested in simulation and a series of phantom tests. Following this, a set of tests are performed on healthy volunteers. The performance of the control system's predictions are tested against a theoretical perfect prediction, utilizing information logged by the MRI machine during the acquisition. In order to determine the effect of the subject specific variation, a set of images is analysed using common image processing tools for each volunteer. Finally, a system for measuring the quality of the acquired images is developed, in order to quantitatively compare results with the state of the art. The results of these methods are then discussed in Chapters 4 and 5. In Section 6 conclusions are outlined relating to the purpose of the study, and a final set of recommendations for improving the results were made.

2 Literature Review

2.1 Cardiovascular Physiology

The heart is the organ responsible for pumping blood throughout the body via the cardiovascular system. There are four chambers within the heart. These are the left and right atria and ventricles. De-oxygenated blood flows into the right atrium from the body's venous system. The blood is pumped from the right ventricle into the lungs through the pulmonary arteries and then returns to the left atrium. The left atrium empties the oxygenated blood into the left ventricle, from which it is then pumped through the arterial system to the body. Blood supply to the heart muscle (myocardium) itself is provided through the left and right coronary arteries.

The pumping of the heart follows a regular cycle. This cardiac cycle is comprised of periods of contraction (systole) and relaxation (diastole). Electrical nerve impulses control the cardiac cycle and can be accurately measured through the electrodes of an ECG. An illustration of how the electrical impulses of an ECG are used to time MRI cardiac MRI acquisitions is shown in Figure 1. Triggering based on the large R-wave of the ECG signal ensures that all the data required to construct the final MR image are acquired during the same phase of the cardiac cycle.

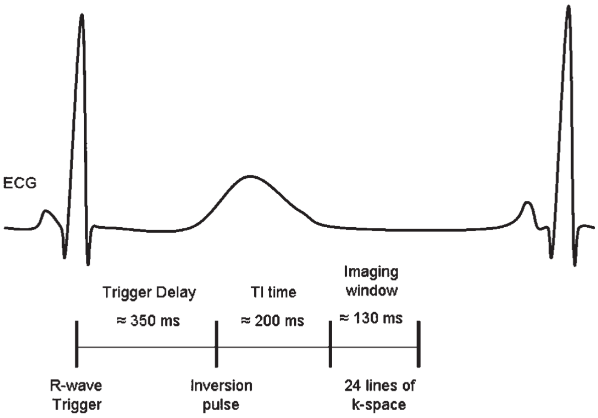

Figure 1: A diagram of the standard delayed enhancement MRI sequence linked to the cardiac cycle.

2.2 Respiratory Motion

Alongside motion due to the cardiac cycle, the heart also moves within the pericardial cavity in the chest during respiration. This motion has been reported as primarily within the inferior-superior direction according to Dey et al. (2010). Since tracking the position of the heart directly is not always viable, due to navigator constraints, the position of the diaphragm can be used as a proxy measure. It is therefore important to understand how the heart moves relative to the diaphragm. A simple linear model is the most commonly used relation between the position of the diaphragm and the heart, with a recommended linear scaling factor of 0.6 (Y. Wang et al., 1995). However, this fails to take into account the three-dimensional nature and hysteresis of the heart motion, which is also subject specific. In order to compensate for these short-comings, Burger and Meintjes (2013) developed an elliptical model, which better predicts the motion of the heart within the chest.

2.3 Respiratory Motion Correction

Initially, cardiac magnetic resonance imaging (CMR) was performed without any respiratory motion correction applied to the images, which introduced noticeable artifacts (Higgins et al., 1985). Improved hardware has increased the speed of acquisition allowing an image (or set of images) to be acquired within a single patient breath hold (10-20 seconds). However, breath holds are often difficult for clinical patients to maintain and repeat reliably, as fatigue sets in during long scanning sessions. Furthermore, the need to keep breath holds short means that there is not always sufficient time to collect the data needed for high resolution scans. It is therefore desirable to remove the need for breath holds from the imaging. Imaging sequences that are capable of correcting for respiratory motion without breath holds are referred to as "free-breathing" sequences.

2.3.1 MRI Navigators

Navigators are widely used to track motion during MRI (Scott et al., 2009). Navigators provide a snapshot image of the position of an anatomical region of interest. Navigators can be one-, two- or three-dimensional. The simplest one-dimensional (linear) navigators in cardiac MRI applications can be used to excite a column of spins along the superior-inferior direction crossing through the right hemidiaphragm. Due to the large difference in contrast between the lungs and the liver, the signal readout along the excited column produces a step-like shape at the lung-liver interface. This step can be detected with a simple edge detection algorithm. Respiratory motion can therefore be tracked during a free-breathing acquisition using repeated navigator measurements. The two most common linear navigators are the crossed pair (Ehman & Felmlee, 1989) and pencil beam navigators (Danias et al., 1997). Crossed pair navigators use a spin echo with the slice selection gradients of the 90°-180° pulses applied to intersecting planes. The intersection results in a rectangular column of refocused spins. In contrast, the 2D pencil beam navigator excites a circular column of spins using a spiral excitation k-space trajectory.

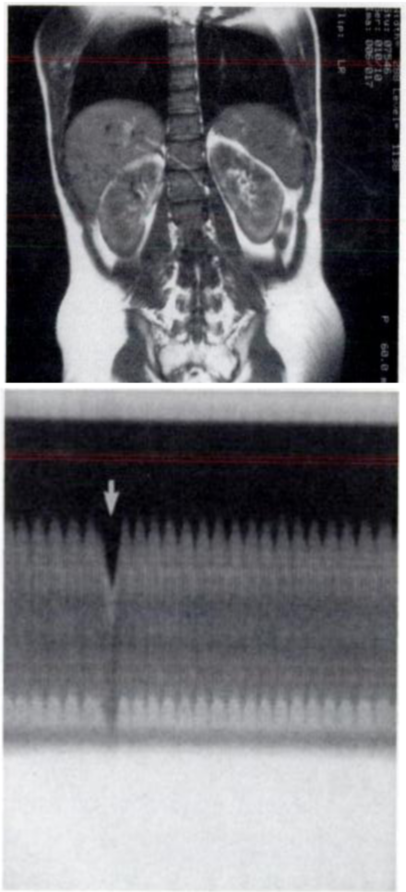

Figure 2: Initial navigator echoes reported by Ehman and Felmlee (1989). Top: Acquisition of the abdomen. The navigator column is not shown, however it has been positioned through the diaphragm in the head-foot direction. Bottom: The navigator images over time; the arrow indicates a momentary deep sigh, which is common in normal respiration.

Navigators are frequently used to provide position information to free-breathing sequences. They may be used to track any object of interest within the acquisition, but the 90°-180°navigators result is saturation effects, leaving a dark column in the final image where they were applied (Ehman & Felmlee, 1989). Because of this, they should not be applied to the tissue area of clinical interest.

2.3.2 Gating Sequences

One approach to compensating for the effects of respiratory motion during free-breathing acquisitions has been the application of gated sequences. These sequences monitor the position of the diaphragm throughout the breathing cycle and only record data when the diaphragm is located within a predefined window. An illustration of this approach is shown in figure 3.

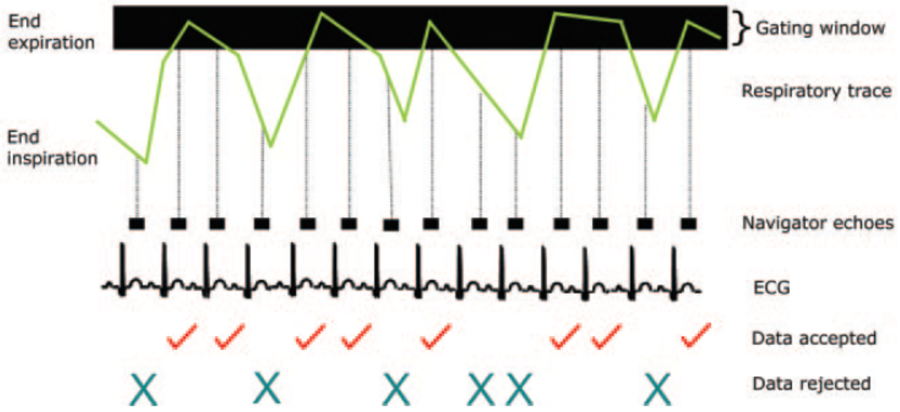

Figure 3: An illustration of the gated sequence process for motion correction (Scott et al., 2009).

Gating methods may employ respiratory bellows (Y. Wang et al., 1995), self-gating signals (Jhooti et al., 2010) or navigator pulses (Ehman & Felmlee, 1989) to track diaphragm motion. Although these methods have been shown to reduce the artifacts produced by respiratory motion, 50% to 70% of all imaging data are rejected. This loss of data results in an increase in the total scan time required. An increase in scan time can be costly in high-demand clinical practices. It is also a limiting factor for acquisitions that are time sensitive, such as delayed contrast enhanced imaging.

2.3.3 Retrospective Motion Correction

Motion correction that is applied after complete or partial image data are acquired, is known as retrospective correction. Restrospective motion correction typically employs various image registration techniques. One early approach applied retrospective motion correction to coronary artery imaging. Hardy et al. (2000) gated the acquisition by registering the artery through adaptive averaging. The method required no patient breath holding, external navigators or ECG-gating but was only 35% efficient in terms of the acquired data that could be used.

Two main forms of image registration are commonly used for retrospective motion correction: rigid and non-rigid registration. Rigid registration preserves the structure of the imaged object by applying only translations and rotations (Crum et al., 2004). However, the variance in human anatomy, especially when considering soft tissues and muscle in motion, require more advanced methods of image transformation in order to register images accurately. These requirements have led to the development of non-rigid transformations, which do not preserve the form of the image. An example of non-rigid image registration for retrospective respiratory gating was applied by Ledesma-Carbayo et al. (2007) to delayed enhancement imaging. Their method removed the requirement for outlining the location of the heart manually, and improved free-breathing image results compared to previous rigid registration methods. Although retrospective correction removes the effects of in-plane motions during the acquisition of the image data, it cannot correct through-plane motion.

A more recent application of retrospective motion correction in MRI was performed by Küstner et al. (2019), wherein deep learning frameworks were retrospectively applied to motion-affected MR images. This method removes motion without the need for a-priori knowledge of the type of motion causing the image artifacts. The deep learning framework was trained with sets of motion-affected and unaffected images. The resulting motion-corrected images were reported as near-realistic motion free images by blinded subjective assessment. However, the final corrected image can sometimes hide anatomical features and is therefore not yet clinically applicable.

2.3.4 Prospective Motion Correction

In order to solve the issues of efficiency and efficacy in removing artifacts due to respiratory motion in CMR, prospective motion correction techniques have been developed. In prospective motion correction, the position of the image slices is adjusted in real-time, thereby ensuring that image data are consistently being acquired from the correct anatomical position. To guide the slice positioning in prospective image compensation, a signal relating the position of the heart to the respiratory motion of the subject is required.

Initial tracking of respiration motion utilized a diaphragmatic navigator and a generalized tracking factor of 0.6 (Y. Wang et al., 1995). This simple approach does not account for patient variation, the complete three-dimensional motion of the heart or the observed hysteresis of the patient whilst breathing (Taylor et al., 1999). Patient specific elliptical (Burger & Meintjes, 2013) and polynomial models (Bush et al., 2019) have shown to produce improved estimates of the position of the heart relative to the diaphragm position.

An early limited form of prospective correction was demonstrated by McConnell et al. (1997). The method utilised navigators to prospectively measure the position of the diaphragm once per cardiac cycle. The heart position is then computed from the diaphragm position using the linear method proposed by Y. Wang et al. (1995), which allowed for adaptive correction of the image location to track the heart. The motion correction resulted in a 47% reduction in slice registration error, within the craniocaudal axis compared to standard breath holding. This technique results in a reduction in through-plane motion and improves the efficiency of the acquisition.

A separate method of prospective tracking implemented by Burger (2012) used a predictor-observer based control system. This system uses a sampling train of initial navigator signals as input to a control system to generate a patient specific respiratory model. Navigators are then repeatedly acquired during the non-imaging segments of the sequence to update the control system. The output of the control system predicts the position of the diaphragm during the imaging segments when navigators cannot be acquired.

2.4 Control System Theory

2.4.1 State Space Models

The control system used for this research is a standard discrete time predictor estimator (Burger, 2012). This control system compares sensor readings of a real-world system to a mathematical model to predict how the real-world model will behave in the immediate future. The error between the model's predicted state and the measured real-world state is then fed back into the model, and the model is altered to minimize the error of future predictions.

The mathematical model commonly used for these control systems is a state space representation. State space representations model the system as a set of inputs, outputs and states, which are related by a set of differential equations. For a continuous linear time-invariant system (LTI) the general state space equations are:

$$\dot{x}(t) = \boldsymbol{A}x(t) + \boldsymbol{B}u(t) \tag{1}$$

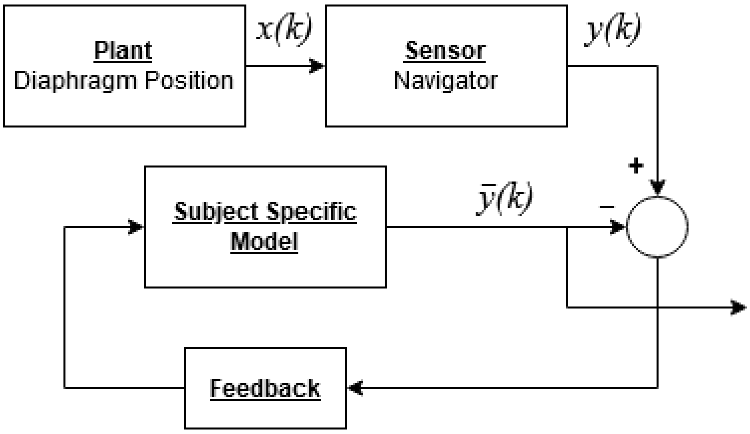

Figure 4: Block diagram of a predictor estimator control system. $x(k)$ is the current state of the plan, $y(k)$ is the current output vector state and $\bar{y}(x)$ is the output vector of the model

$$y(t) = \boldsymbol{C}x(t) + \boldsymbol{D}u(t) \tag{2}$$

When a discrete system is considered, the equations 1 and 2 are altered such that:

$$x(k+1) = \boldsymbol{A_d}x(k) + \boldsymbol{B_d}u(k) \tag{3}$$

$$y(k) = \boldsymbol{C_d}x(k) + \boldsymbol{D_d}u(k) \tag{4}$$

Where: $\boldsymbol{A_d} = e^{AT}$, $\boldsymbol{B} = \boldsymbol{A}^{-1}(\boldsymbol{A_d} - \boldsymbol{I})\boldsymbol{B}$, $\boldsymbol{C_d} = \boldsymbol{C}$, $\boldsymbol{D_d} = \boldsymbol{D}$ and T is the sampling period for the sensors. The exponential term, e^{AT}, is approximately equal to $\boldsymbol{I} + \boldsymbol{A}T$ for sufficiently small sampling periods. Furthermore, for small T, equation 3 becomes:

$$x(k+1) = \boldsymbol{\Phi}x(k) + \boldsymbol{\Gamma}u(k) \tag{5}$$

where $\boldsymbol{\Phi} = \boldsymbol{I} + \boldsymbol{A}T$
and $\boldsymbol{\Gamma} = \boldsymbol{A}^{-1}(\boldsymbol{\Phi} - \boldsymbol{I})\boldsymbol{B}$

2.4.2 Predictor-Observer Model

When the internal state of the real-world system cannot be directly measured, exact state feedback is not possible. In this case, if a mathematical expression between a signal that can be measured and the actual internal state exists, this expression can be used as an “observer’ to the actual internal state. The current sequence makes use of navigators which saturate the tissue when imaged, resulting in void spaces in the image. Therefore, instead of measuring the heart position directly, navigators are placed at the lung-liver interface. However, a patient's breathing may vary over the duration of the scan, becoming slower as they relax for example. This variation results in an error in the observer model, which can be minimized through feedback with the control system.

Mathematically the observer can be included within the standard control state space equations by updating equations 3 and 4 as follows:

$$\hat{x}(k+1) = \mathbf{\Phi}\hat{x}(k) + \boldsymbol{L_p}\tilde{x}(k) \tag{6}$$

$$\hat{y}(k) = \boldsymbol{H}\hat{x}(k) \tag{7}$$

$$\tilde{x}(k) = y(k) - \hat{y}(k) \tag{8}$$

In the above equations, $\hat{x}(k)$ is the current estimated state of the real-world system, $\hat{x}(k+1)$ is the predicted future state of the system, $\hat{y}(k)$ is the output of the model. $\boldsymbol{H}$ is the output matrix, and $\boldsymbol{L_p}$ is the observer matrix. The observer matrix alters the sensor input and can be tuned higher or lower depending on reliability of the sensor.

2.4.3 Breathing Model

Burger (2012) demonstrated that a sinusoidal relationship accurately represents the motion of the diaphragm. The relationship is given by:

$$f(t) = sin(\alpha t) \tag{9}$$

where $\alpha = 2\pi\omega$ and ω is the breathing frequency.

Transforming 9 into the frequency domain through the Laplace transform yields the following:

$$f(t) = sin(\alpha t) \xrightarrow{\mathcal{L}} \frac{\alpha}{(s^2 + \alpha^2)} = F(s) \tag{10}$$

The transfer function of the model, $F(s)$, is the ratio of the output of the system to the input, $F(s) = \frac{Y(s)}{U(s)}$. This can be rearranged to solve for $Y(s)$ such that:

$$s^2Y(s) = -\alpha^2Y(s) + \alpha U(s) \tag{11}$$

$$\{\mathcal{L}\}^{-1} \implies y(\ddot{t}) = -\alpha^2y(t) + \alpha u(t) \tag{12}$$

The time domain representation can then be arranged into the state space form. Setting $u = 0$ and substituting $\dot{y} = x_1$ and $y = x_2$, the following model can be formed:

$$\begin{bmatrix} \dot{x_1} \\ \dot{x_2} \end{bmatrix} = \begin{bmatrix} 0 & -\alpha^2 \\ 1 & 0 \end{bmatrix} \begin{bmatrix} x_1 \\ x_2 \end{bmatrix} \tag{13}$$

Equation 1 shows the relationship between the current estimated state of the system and the predicted state. Therefore $A = \begin{bmatrix} 0 & -\alpha^2 \\ 1 & 0 \end{bmatrix}$. The discrete equivalent $\mathbf{\Phi}$ can be calculated:

$$\mathbf{\Phi} = \boldsymbol{I} + \boldsymbol{A}T = \begin{bmatrix} 1 & -\alpha^2T \\ T & 1 \end{bmatrix} \tag{14}$$

In order to set $\hat{y}$ to the current state, x_1, a suitable $\boldsymbol{H}$ must be selected as per equation 7.

$$\boldsymbol{H} = \begin{bmatrix} 1 & 0 \end{bmatrix} \tag{15}$$

2.4.4 Loop Feedback Characteristics

Finally, the values for the estimator feedback gain characteristics, $\boldsymbol{L_p}$, can be calculated by first specifying the desired estimator pole locations in the z-plane:

$$(z_1 - \beta_1)(z_2 - \beta_2) = 0 \tag{16}$$

Where each β is a complex number representing a desired estimator pole location and affect the speed at which the estimator converges with the plant (system under study). Powell and Franklin (1998) have shown that the characteristic equation for the predictor-observer is:

$$|z\boldsymbol{I} - \boldsymbol{\Phi} + \boldsymbol{L_p H}| = 0 \tag{17}$$

2.5 Image Analysis

2.5.1 Image Morphology

Morphology transformations are a common image processing method used to aid the detection of edges and de-noising (Mehena, 2013). Morphological transformations often take in binary images and a kernel as inputs. These inputs are then combined using mathematical set operations (intersection, union, inclusion, complement) (Robert Fisher et al., 2003). Although these methods are designed to work on various grayscale levels, the images within this project will be converted to binary values (one or zero everywhere) and the default set of morphological functions will be used. Commonly, high value regions in the binary image are referred to as the foreground and low values regions as the background.

The two basic operations of morphology are erosion and dilation. All morphological operations utilize a grid of pixel locations, known as the image kernel. This grid of locations specifies the region of pixels to consider when applying the morphological operation to the image. In the case of erosion every foreground pixel in the input image is processed one-by-one. For dilation, every background pixel is considered instead. For each pixel the kernel is positioned with the sample image pixel at the center of the kernel. From there, every sample image pixel that overlaps with the kernel is considered for either erosion or dilation. In the case of erosion, if any overlapping pixel is in the background (zero value) then the input image pixel is also set to zero. This is reversed for dilation, where if any of the overlapping pixels are in the foreground (non-zero value) then the input image pixel is set to non-zero (foreground). The effective result is that for erosion, any pixel not surrounded by foreground is set to background, and vice-versa for dilation.

A sample process of erosion and dilation is shown in Figure 5.

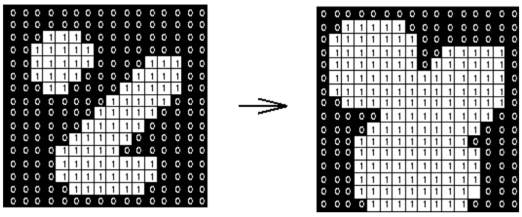
Dilation by a 3x3 Kernel

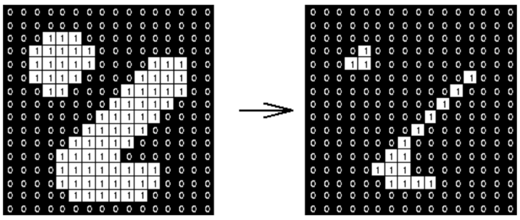
Erosion by a 3x3 Kernel

Figure 5: Sample images illustrating the effect of dilation and erosion on the image foreground (Robert Fisher et al., 2003)

The dilation and erosion functions are useful for edge detecting and noise reduction when applied one after the other along with some extra processing. A dilation operation followed by an erosion operation is known as a closing operation, as it has the effect of removing small holes within a sample image. An erosion operation followed by a dilation is known as an opening operation. It is useful in removing noise.

Morphological transformations are used to remove noise and highlight edges when tracking both the heart and diaphragm. The functions were implemented using the open computer vision (openCV) package (Bradski, G, 2000). Examples of opening and closing results are shown in Figure 6.

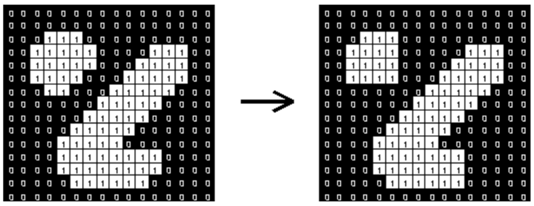
Opening with a 3x3 Kernel

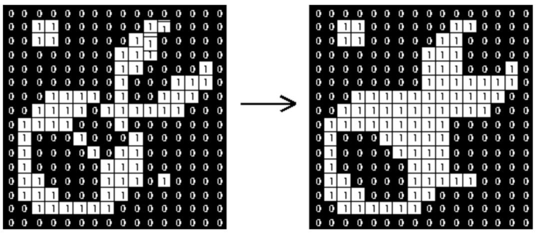
Closing with a 3x3 Kernel

Figure 6: Sample images illustrating the effect of opening and closing image foreground (Robert Fisher et al., 2003).

2.5.2 Image Quality Assessment

Medical Image Quality Assessment (MIQA) is important to quantify the success of all new medical imaging sequences. As such, there are many well known and standard methods for assessment. Broadly, there are two main groups of IQA: direct and indirect.

Direct and Indirect Analysis Direct assessment requires that there exist some ground truth high-quality image to compare the experimental image against. Indirect analysis is designed work independently, and identify those with higher noise and distortions without any reference images.

Indirect analysis does not require comparison between images. Instead calculations are applied to a single image. An independent global scale for the indirect measure's score is provided. A score for each image can then rank the quality of a single image against the global scale rather than a reference. A common algorithm used for indirect IQA is the Blind/Referenceless Image Quality Evaluator (BRISQUE). The quality metric output for BRISQUE is a number from 0 to 100, with 0 being the ideal score and 100 the poorest. However, it is worth noting that the BRISQUE measure was developed specifically for use in measuring the quality of natural images. Natural images in this context do not necessarily require nature, such as trees or skies, but rather any image taken with the use of an optical camera. As such, it is not readily apparent that the measure will be suitable for MR images. However, Yu et al. (2018) have reported evidence that BRISQUE is sufficiently able to score the quality of MR images when compared with standard IQA measures used for brain MR imaging. This provides some basis for applying this quality measure to the cardiac MR images collected for this study.

Two Sample Analysis Another method of quality assessment proposed by NEMA (National Electrical Manufacturers Association, Standard MS 1-2001 (Rosslyn, 2001)). compares two regions of interest within an image - a region within the tissue (signal) and a region of empty space (noise). It is therefore referred to as the two sample analysis method. The calculations used to calculate the two sample peak signal-to-noise ratio (pSNR) are based on research published by Dietrich et al. (2007).

3 Research Methodology

The main aim of this dissertation was to implement and validate a novel prospectively motion corrected FLASH sequence for free-breathing cardiac MRI. Firstly the control system's mathematical models was tested in isolation. Following this validation the FLASH sequence was modified within the Siemens IDEA (Integrated Development Environment for Applications) platform. After validation of the modified sequence in simulations, the sequence was tested using imaging phantoms and with healthy volunteers. Multiple acquisitions were performed to compare the standard techniques (namely breath-held and free-breathing gated) to the proposed control system method. Finally, various image processing techniques were applied to compare the image quality for the different acquisitions.

3.1 Control System Adapted Sequence Development

3.1.1 Sequence Development

Observer Predictor Controller

Initially the controller predictor model was validated in a MATLAB simulation. Real breathing data were gathered from navigators placed on the diaphragm. The breathing data were used as test input into the control system model to validate the configuration and parameters. The two poles for the controller listed in equation 16, z_1 and z_2, were thus calculated experimentally.

Control Protocol Development

The control system implementation was developed by adapting existing FLASH C++ code provided by SIEMENS for research. The SIEMENS IDEA platform supports development and simulation of various MRI protocols. The platform was used to refine and validate the timings and calculations of the control system.

The original process flow for the SIEMENS gated FLASH sequence is displayed below in Figure 7.

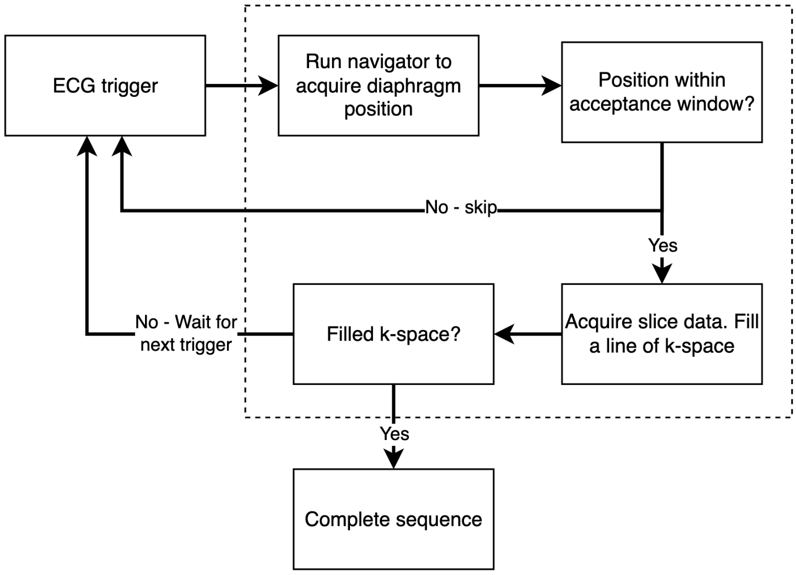

Figure 7: Flow diagram showing key processes of the gated FLASH sequence.

A control system that samples state information rather than processing continuous analog signals is a digital controller. It is vital that a digital controller's sample period, T_s, remains as close to constant as possible. Inconsistent sample rates have been shown to effectively introduce unexpected low and high pass filters into the controller's frequency response (Kuruppu & Shibilski, 2019). Thus, the parameters of the control system model were calculated with a constant sample rate. The original gated FLASH sequence would run one navigator prior to the excitation only. Initially, we tried to fit as many navigators as the timing would allow. Since this led to inconsistencies in the spacing between navigators, our final implementation maintained a fixed sample rate between the navigators.

A fixed sample rate of 100ms was used. Lower sampling rates were theoretically possible but were prevented by technical constraints. The 100ms rate provides enough time to read the navigator position, whilst providing buffer time for miscellaneous processing.

Additionally, the duration of the kernel for the FLASH sequence (the imaging segment) and the delays between ECG triggers are variable. Thus, buffer times were added and certain navigators were skipped if there was insufficient time to collect a navigator read-out within the 100ms. The skipped navigators could then be estimated using the predictions from the control system.

As it is not possible to collect the navigator points during imaging, the control system is used to predict points where navigators would have occurred. These points are spaced at the same 100ms sample rate as the standard navigators. The remaining positions could then be obtained through linear interpolation between the predicted positions. An illustration of the points used for interpolation is shown in Figure 8:

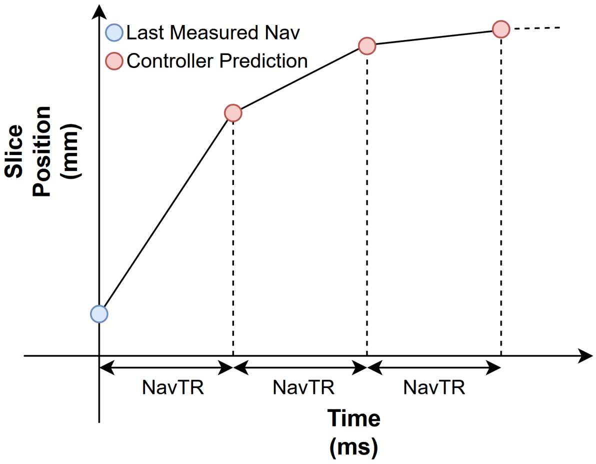

Figure 8: Linear interpolation from positions predicted by the control system.

For each period between controller predictions during the imaging segment, positions were determined using a simple line equation $y = mx + c$, where $m = \frac{y(t)-y(t-1)}{navTR}$, $c = y(t-1)$ and $navTR$ is the navigator repetition time (ie. 100ms in the current implementation). A linear interpolation between points was deemed satisfactory rather than higher polynomial estimates, as these sections of estimation are providing granular predictions to existing controller predictions and over very short periods of time. Along with this, given that motion of breathing is largely sinusoidal, large segments of the motion are closely approximated as linear.

A flow diagram of the control system adapted sequence is shown in Figure 9. Important additions are the initial 256 scout navigators, which are used to provide enough data to calculate the frequency of the tidal breathing and calculate the median position of the diaphragm during breathing.

While some parameters of the control system can be calculated offline before any implementation, others are dynamic and based upon each specific subject's breathing pattern. Most notable of these is the frequency of the breathing. This was represented by α in the initial mathematical description of the control system mathematical derivation in equation 9. The initial 256 navigator positions provide the data necessary to calculate the breathing frequency for the subject via a Fast Fourier Transform (FFT). The FFT is a commonly used digital implementation of the Fourier Transform, and maps sampled time data into fundamental frequency components. The dominant breathing frequency of the subject is the highest amplitude component with the lowest frequency range. Noise

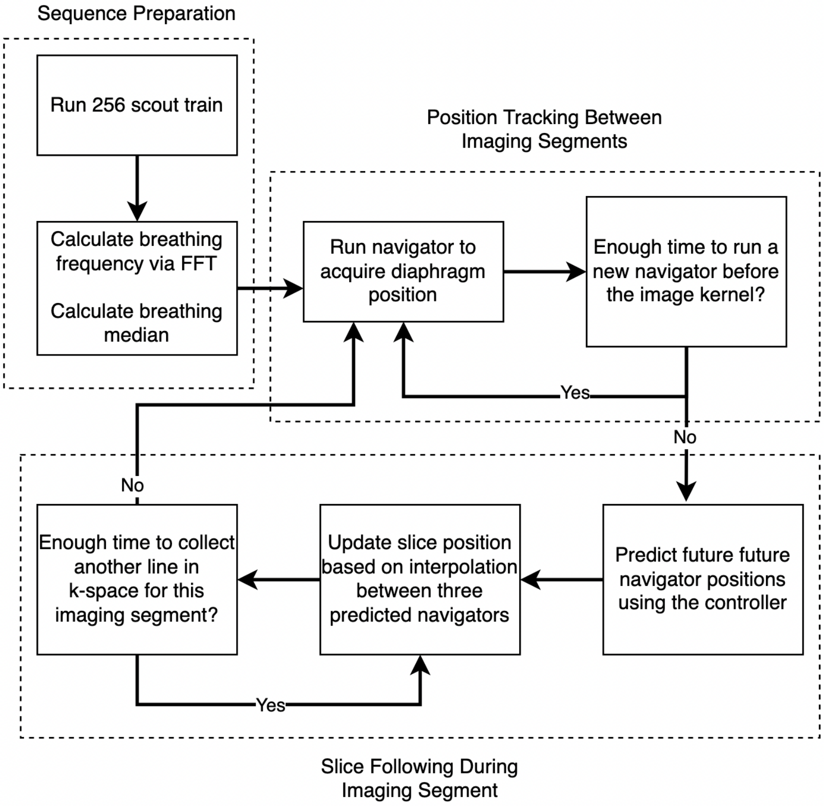

Figure 9: Flow diagram outlining stages in the adapted FLASH sequence.

related to the navigator data are significantly higher frequency than the base breathing frequency. Figure 10 displays an example FFT applied to sampled breathing data. In this example, the frequency component with the largest amplitude, indicated in the bottom sub-plot, is 0.31Hz. This equates to one full respiratory cycle over 3.2 seconds or 18.75 breaths per minute.

Alongside the FFT of the initial 256 scout samples, the median of the values was calculated. The median is an important measure for the operation of the system as all controller errors are relative to the previous slice position. In contrast, the positions provided by the navigator readings are relative to the bottom of the navigator field-of-view. It was assumed that the sinusoidal nature of tidal breathing would contain a consistent median value. This median value is equivalent to applying an offset bias to the sinusoid. In Figure 10 this offset value is approximately 125mm. The median is therefore subtracted from the controller's predicted position to determine the shift that needs to be applied to move the slice to the predicted position.

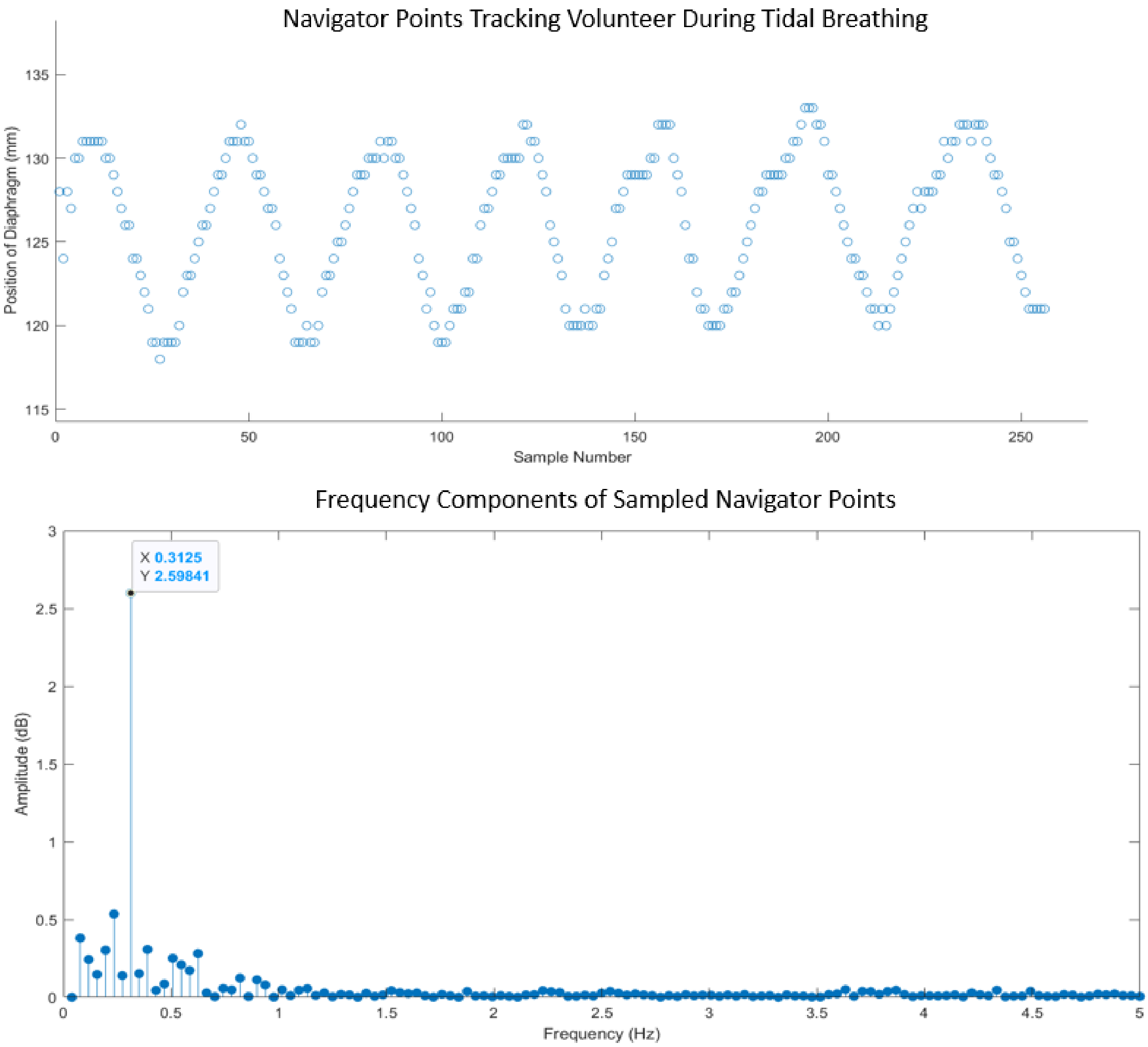

Figure 10: Figure showing an example fast fourier transform of sample breathing position data. Top: Sampled tidal breathing, showing it's sinusoidal nature and the navigator position offset bias. Bottom: Frequency components of the sampled breathing data.

3.1.2 Simulation Testing

Beyond initial mathematical model testing, further simulation testing was performed utilizing the SIEMENS IDEA platform. This allowed for both development and simulation of the actual C++ code which would be run on the MRI machine. The simulation of the acquisition was altered to allow for inputs of navigator data, which was then used to validate the operation of the control system and test its response time and accuracy.

In order to test the control system's ability to predict the motion of tidal breathing, a sampled sine wave was used as input to the simulator. The number of navigators in the standard FLASH sequence is dynamic between imaging segments based upon the heart-rate and trigger delay. Within the simulation a steady heart rate of 60bpm was chosen, which leads to a set number navigators between imaging segments. Sections of data were removed from our test sine wave to match the loss of navigator data during the imaging segments as expected during an actual acquisition.

As shown in Figure 11, the control system accurately predicts the navigator positions(shown in red) for sections where navigator data (in blue) are missing.

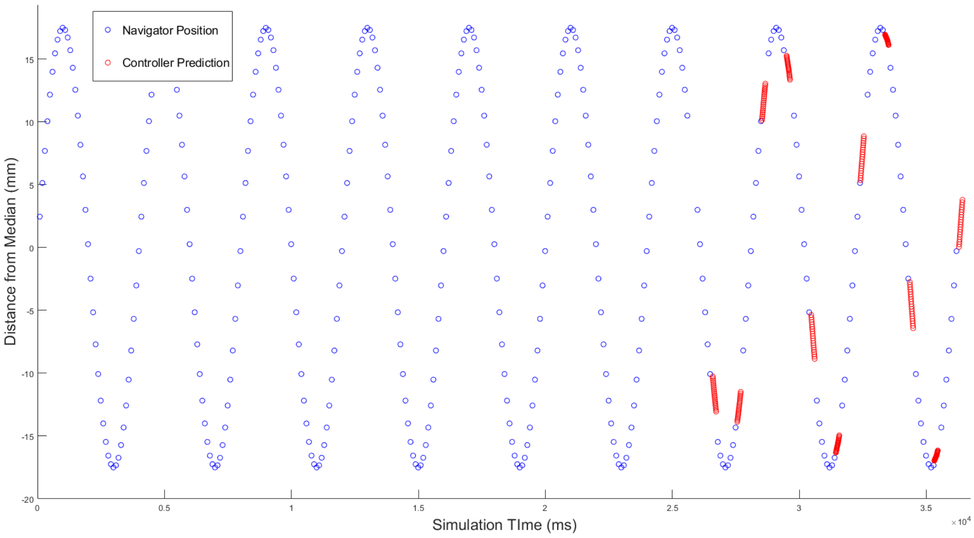

Figure 11: Plot of simulated sinusoidal navigator positions (in blue) and associated controller predictions (in red). This plot includes the initial 256 navigators used to estimate the median position and the frequency of the motion, which are required by the controller.

3.2 Image Acquisition

3.2.1 Phantom Testing

Before testing on human subjects, the sequence performance was tested with a liquid phantom. The phantom was placed in a motion rig that emulates tidal respiratory motion. An image of the motion rig is shown in Figure 12.

The handle at the bottom of the motion rig is cranked in a circular motion. This rotation of the crank is translated 90 degrees by a bevel gear. A platform at the end

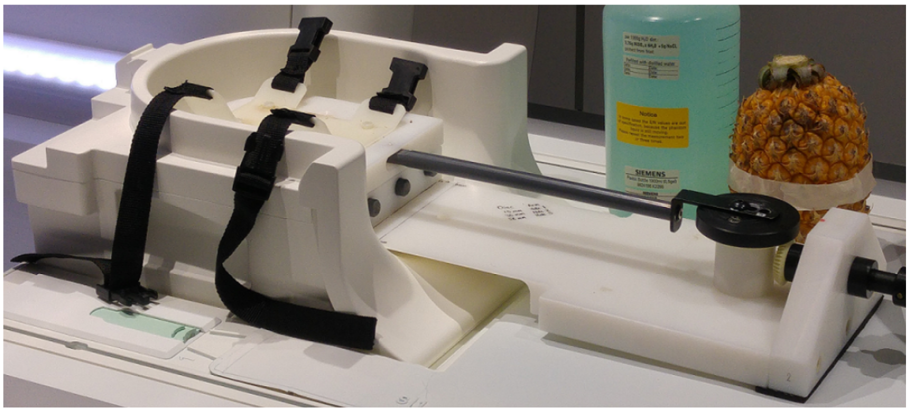

Figure 12: Motion rig used to simulate tidal respiratory motion in the superior and inferior directions.

of the rig is then driven through superior and inferior directions by a shaft attached at an offset to the bevel gear. This shaft therefore translates a sinusoidal motion to the platform. It is important to note that the motion rig is only able to fit within the neck-head imaging coil, rather than the body coil that is typically used for cardiac MR.

For all of these phantom tests, the linear tracking factor was set to 1 rather than the usual 0.6-0.7. This is because the navigators for these tests can be applied directly to the edge of the phantom and therefore the positions reported by the navigators directly relate to the position of the phantom. In order to better understand the impact of the image artifacts due to the motion, a vitamin oil capsule was taped to the side of the phantom, at the midway point. This provided contrast to the image and a point of localization when imaging in different planes.

A further set of test images were acquired of a pineapple in the respiratory motion rig. Although similar in shape to the test phantom, the pineapple contains a detailed internal structure. This internal structure is beneficial for determining the quality of the acquired images.

3.2.2 Volunteer Testing

Acquisition Protocols

Data from nine healthy volunteers (aged 26 ± 2.6) were used to analyze the quality of images acquired using the control-adapted FLASH sequence. However, data acquired from volunteer 1 was discarded as a fault was discovered in the operation of the modified sequence, which was fixed for the remaining volunteers.

The acquisition protocols and associated parameters are shown in Table 1.

Table 1

Acquisition protocols

Protocol Name	**TR/TE**	**Flip Angle**	**FOV**	**Matrix Size**
Breath-held (BH) FLASH	127.5/3.33	20	340	192x192
Free-breathing (FB) FLASH No Motion Correction	127.5/3.33	20	340	192x192
Gated FLASH 4mm Acceptance Window	127.5/3.33	20	340	192x192
Control System (CS) Adapted FLASH	127.5/3.33	20	340	192x192
Cine FLASH 50 Acquisitions	86.24/2.9	20	340	256x256

All scans were performed on the Siemens Skyra using an 18 channel body coil and 32 channel spine coil. All protocols were run in three different orientations: sagittal, axial and coronal. For each of these orientations, the control system adapted protocol was repeated three times with varying tracking factors of 0.6, 0.65 and 0.70.

3.3 Analyses

3.3.1 Control System Prediction Accuracy

A method was developed to quantitatively analyze the accuracy of the control system outputs. The accuracy of the control system's predictions depend upon how closely predicted the diaphragm positions during the imaging match the actual positions of the diaphragm. However, there is no recorded true position of the diaphragm for the entire sequence, as navigator information is not available during the imaging segment. Therefore, an estimate of the true position of the diaphragm during the imaging segment is required. The position of the diaphragm between the imaging segments is available and can be used for this estimation.

A third degree polynomial estimation was used between each imaging segment for this purpose. The input data to the polynomial fit were gathered from navigator values both before and after the imaging segment. Therefore, the estimate is based upon "future" information that would not be available to the controller at the time of operation. This allows the polynomial estimate to better approximate the most likely position of the diaphragm. A third-degree polynomial $p(x)$ takes the following form:

$$p(x) = p_1x^3 + p_2x^2 + p_3x + p_4$$

Where p_1, p_2, p_3 and p_4 are the parameters which are altered to best fit $p(x)$ to the data.

In order to fit the polynomial, 8 navigator positions before and after the imaging segment were used. These points were input into the MATLAB `polyfit` function to calculate the best fit parameters for the polynomial equation.

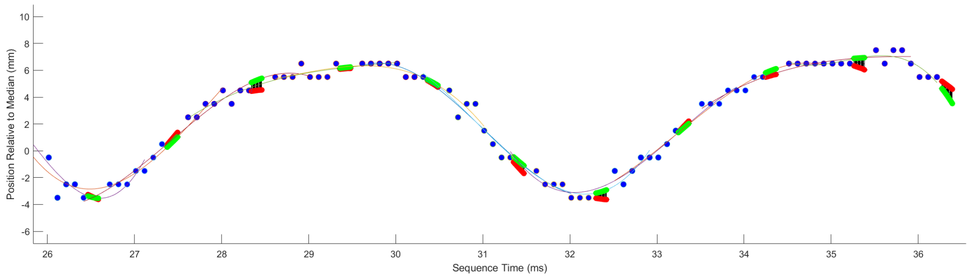

Figure 13: Plot showing three dimensional polynomial estimations of diaphragm displacement (in green) compared with displacements predicted by the controller (in red).

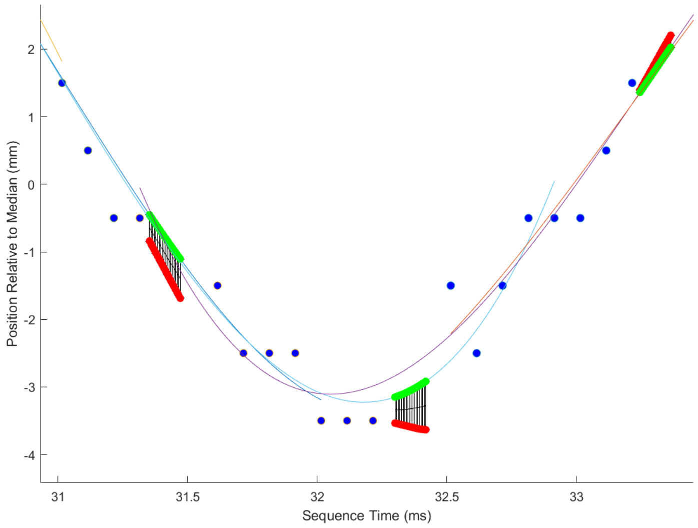

Figure 14: Subsection showing two seconds of diaphragm positions measured by the , predicted controller positions, and three dimensional polynomial estimates of navigator positions.

A set of polynomial approximations was created for each imaging segment within the acquisition. Since the set of points in time, t_p, used for fitting the polynomial match the acquisition sequence time in milliseconds, the result of the polynomial for the same points in time, $p(t_p)$, at some sequence time t provides a best estimate for the displacement of the diaphragm. It is then simple to compare the diaphragm displacement predicted by the control system at time t_c ($con(t_c)$) with that estimated by the polynomial fit at the same time t_c ($p(t_c)$). The approximate error $\tilde{e}(t_c)$ of the control system's prediction is given by the difference between the two: $\tilde{e}(t_c) = p(t_c) - con(t_c)$. The error for every point predicted by the controller throughout the acquisition can then be used to provide a quantitative measure of the accuracy of the control system. A common measure for prediction error is the root mean squared error of the predictions. When comparing the control system predictions to the polynomial fit estimations we are able to calculate the RMSE using:

$$RMSE = \sqrt{\frac{\sum_{t=1}^{T}(p(t) - con(t)^2)}{T}} = \sqrt{\frac{\sum_{t=1}^{T}\tilde{e}(t)^2}{T}} \tag{18}$$

3.3.2 Image Quality Assessment (IQA)

Direct Analysis

For direct analyses, the breath-held images were considered the ground truth. The list of direct assessment measures that were tested against the volunteer acquisitions are outlined in Table 2.

Table 2
Table of direct assessment measures. Including score ranges and ideal scores.

Metric Name	**Score Range**	**Ideal Score**	**Citation**
MSE - Mean Squared Error	0 - inf	0	N/A
RMSE - Root Mean Squared Error	0 - inf	0	N/A
Direct pSNR (Peak Signal-to-Noise Ratio)	0 - inf	inf	(A.C. Bovik et al., 2004)
UQI - Universal Quality Index	0 - inf	inf	(Z. Wang & Bovik, 2002)
SSIM - Structural Similarity Index	0 - inf	inf	(A.C. Bovik et al., 2004)
ERGAS - Erreur Relative Globale Adimensionnelle de Synthèse	0 - inf	0	(Wald, 2000)
SCC - Spetail Correlation Coeffecient	0 - 1	1	(Zhou et al., 1998)
SAM - Spectral Angle Mapper	0 - 1	0	(Yuhas et al., 1992)
RASE - Relative Average Spectral Error	0 - inf	0	(Gonzalez-Audicana et al., 2004)
SCC - Spatial Correlation Co-efficient	-1 - 1	1	(Sheikh & Bovik, 2006)

Due to the calculations relying on direct comparisons between exact pixels or neighborhoods of pixels, and the presence of black saturated bands perpendicular to the lung-liver interface from navigators on the free-breathing gated and control system acquired images that are not present on the non-navigated images (Figure 15), results from direct analyses may not reflect the quality of the image around the heart. Moreover, the images acquired using the control system present Moiré interference fringes in the regions superior to the heart that do not impact the image quality of the heart itself, but lead to poor results on direst assessment measures.

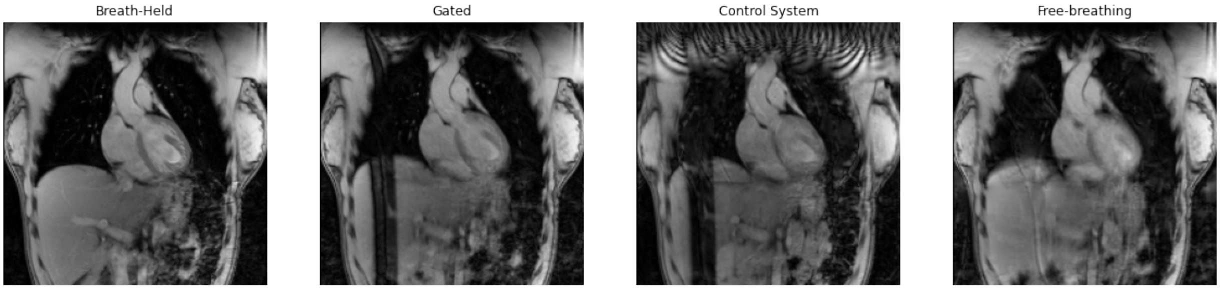

Figure 15: Example coronal acquisitions for a single volunteer.

To obtain more reliable measures of the image quality of the heart itself, we applied further direct analysis testing to cropped acquisitions, with the heart at the center and masked to remove all background image data.

Examples of the cropped heart images images are shown in Figure 16.

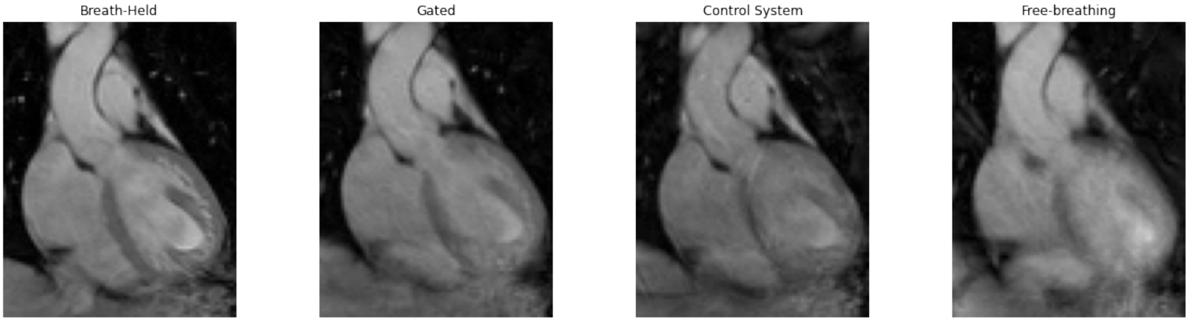

Figure 16: Cropped heart images used for direct image quality assessment.

Figure 17 shows the various stages of the creation of a mask to isolate the heart from the background lung area.

Figure 18 shows examples of the masked heart images for each of the different acquisitions. Note, that when compared with Figure 16, the lung region around the heart has been removed and is now completely black.

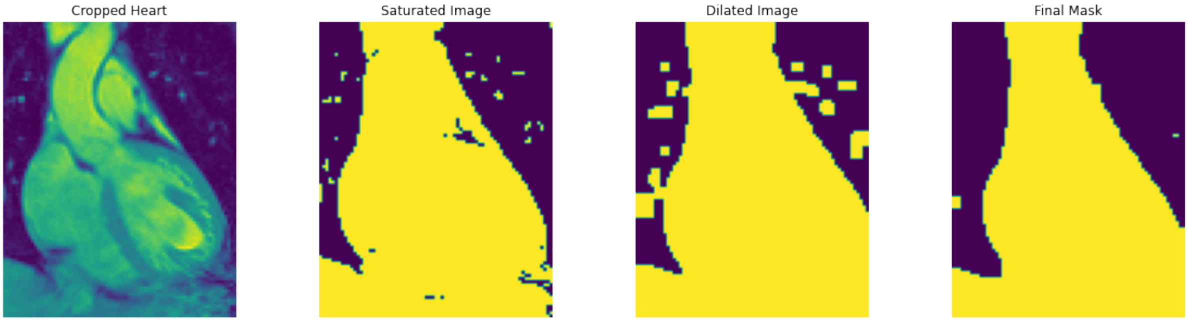

Figure 17: Images showing the process of creating heart isolating masks.

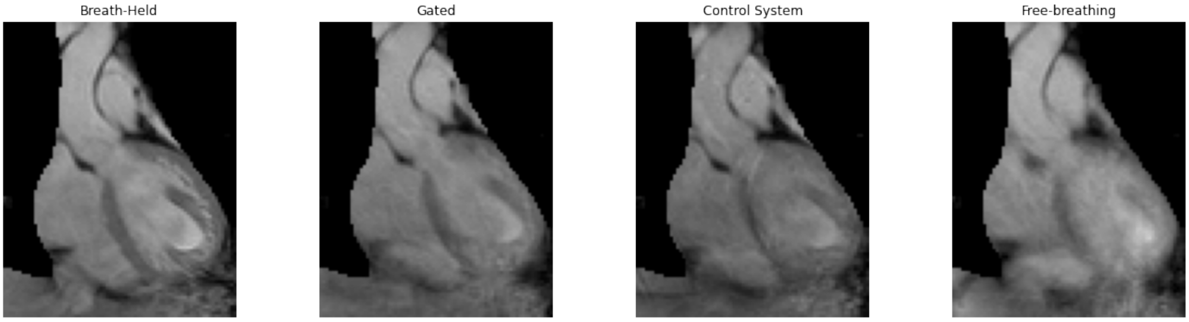

Figure 18: Resulting masked heart images, acquired by applying the mask of Figure 17 to the cropped images of Figure 16.

Indirect Analysis

The indirect quality measure utilized was the Blind/Referenceless Image Quality Evaluator (BRISQUE). Similarly to the direct image quality assessment (IQA), BRISQUE tests were performed across the entire images and the cropped heart images to ensure that there is no impact on the measures due to the saturated navigator regions.

Two Sample Analysis

The two sample method does not require a comparison against a ground truth image and is therefore an example of indirect IQA. For the purposes of this investigation, the tissue sample was selected from the heart region, and the empty space samples in the region right or left of the chest, below the arm (Figure 19).

The calculation of the pSNR (peak signal-to-noise ratio) is defined as the ratio of the mean signal in the tissue ROI and the standard deviation of the signal in the noise ROI. Equation 19 illustrates the final equation used for calculating the pSNR values.

Because this is a signal-to-noise ratio, a higher value indicates more clarity and is therefore desirable.

$$pSNR = \frac{S}{\sigma} = \frac{\underset{r \in ROI_{tissue}}{mean} \left(S_N(r, tissue) \right)}{\sqrt{\frac{2}{4-\pi}} \underset{r \in ROI_{noise}}{stddev} \left(S_N(r, noise) \right)} = \frac{\mu_{image}}{0.655(\sigma_{noise})} \tag{19}$$

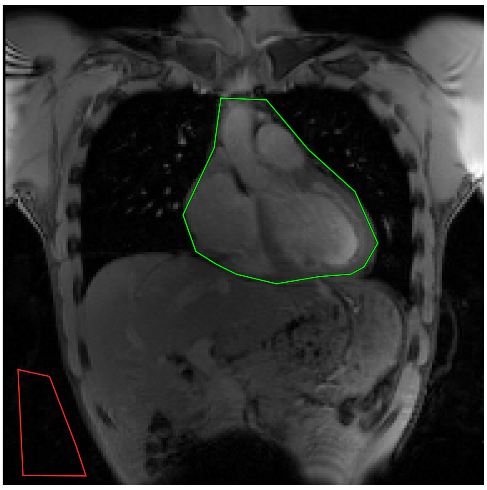

Figure 19: Example regions of interest (ROI) selected for two sample pSNR IQA. (green: tissue ROI, red: noise ROI)

The two sample pSNR scores for each volunteer were then normalized by dividing all of the pSNR scores by the score for the breat-held acquisition. This sets the pSNR value for all volunteer breath-held acquisitions to 1, thus serving as the base truth. This allows for comparison of the scores of the different acquisitions between volunteers.

3.3.3 Analyses of Tracking Factor Variability

It has been shown that the relation between displacements of the lung-liver interface and the heart, known as the tracking factor, is subject specific and non-linear (Burger & Meintjes, 2013). The tracking factor used in the current implementation of the control system adapted sequence is a static linear value throughout the acquisition. This is currently the standard practice in free-breaking slice-following sequences. To understand how inter-subject tracking factor variability impacts the quality of the images acquired and the accuracy of the control system sequence, we directly measured the tracking factor for each volunteer from a set of low resolution cine images.

Diaphragm Tracking From Cine Images

Each image was first segmented by amplitude clustering into a binary image. Amplitude clustering is the process of assigning a range of signal values in an image the same value. For edge detection, clustering into two binary groups provides the best contrast. Amplitude clustering is effective in cardiac MRI acquisitions as there is already a strong contrast between the air in the lungs and other tissues.

Following this, the image was cropped twice to highlight the diaphragm and the heart separately. Each cropped segment was then morphologically closed to remove the small clusters of outliers that remained from the original crude amplitude clustering. The results of one such morphological closing are shown in Figure 20.

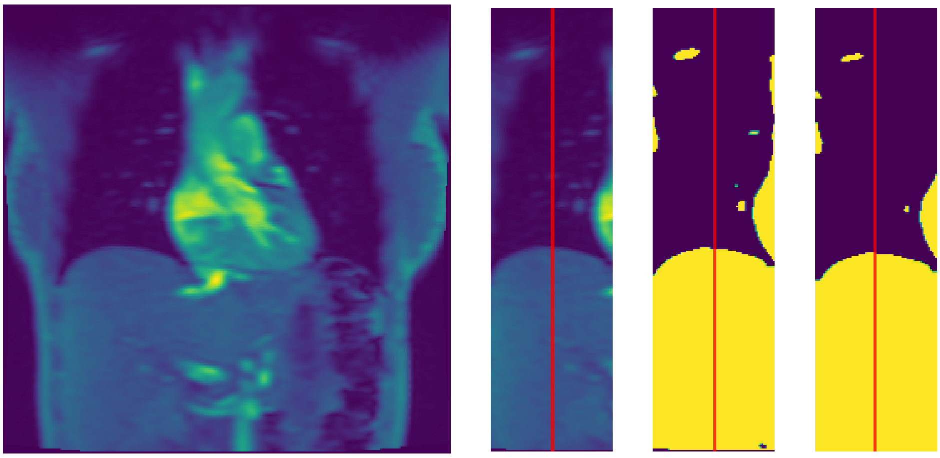

Figure 20: (Left) Sample image from the coronal cine acquisition. Cropped sections to the right illustrate morphological closing and the location of lung-liver edge used for tracking (red line).

A single pixel width column was then sampled along the vertical axis of the image (red line in Figure 20). The slice was positioned over the apex of the lung-liver edge. The position of the edge was determined by detecting the rising edge in the slice, which indicates the change in amplitude between the lung and the liver. The tracked diaphragm position for a single volunteer can be seen in Figure 21 below.

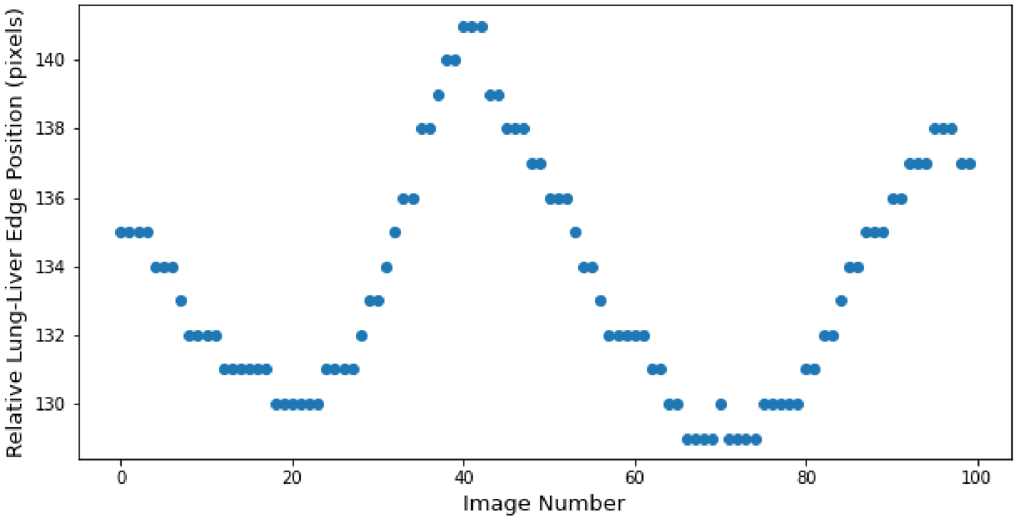

Figure 21: Scatter plot showing how the position of the lung-liver edge changes throughout the cine acquisition.

Heart Tracking from Cine Images

Unlike the lung-liver interface, The heart does not have a clear high contrast edge. It also deforms non-rigidly during respiration. As such, multiple methods of tracking the position of the heart were tested. Two of these methods utilize generic image tracking algorithms available in the openCV (open computer vision) framework. The two tracking methods used were the multiple instance learning (MIL) tracker and the Kernalized Correlation Filter (KCF) tracker. Both tracking algorithms are specifically designed for general tracking of objects. The third method used a sample line for the edge detection tracking. The line was positioned through the left ventricle, to the right of the left atrium, as shown by the vertical line in Figure 22.

An example of the results of the three methods is shown in Figure 23.

Although all three methods tracked the position of the heart successfully, the direct trace below the left atrium provided the least noisy measure. Therefore the direct trace was used to measure the motion of both the lung-liver interface and the heart throughout the cine acquisitions.

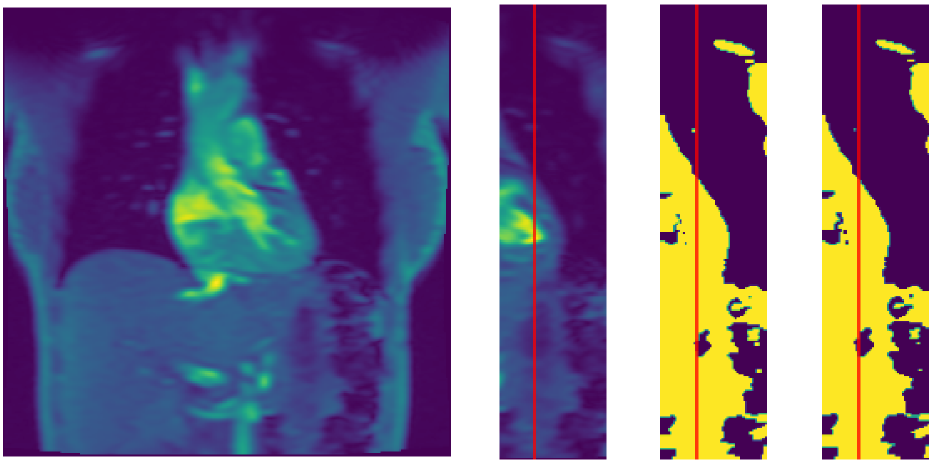

Figure 22: Sample Image Acquisitions of Cine Coronal Acquisitions. Cropped Sections to the Right Illustrate Morphological Closing and Location of Heart Edge Tracking (Red Line).

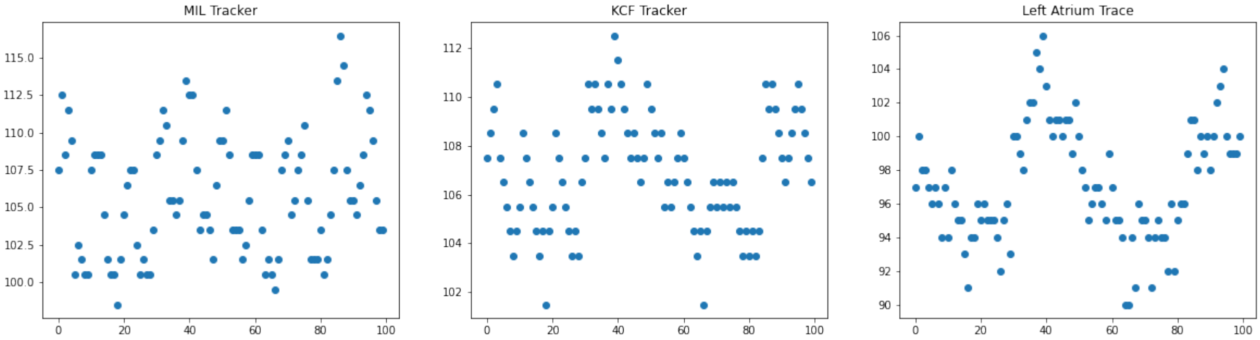

Figure 23: Scatter Plots of Heart Edge Tracking Results.

Tracking Factor Estimation

The edge positions (relative to an origin in the top left corner of the images) of both the heart and lung-liver interface as a function of time, were normalized by subtracting the median of the data. A sinusoidal curve was then optimally fit to the normalized data using the `curve_fit` function in the optimization library of the `sci-py` python framework (Pauli Virtanen, Ralf Gommers, et. al., 2020).

An example of the resulting sinusoidal fits is shown in black in Figure 24, with a single standard deviation of the fit shown in grey.

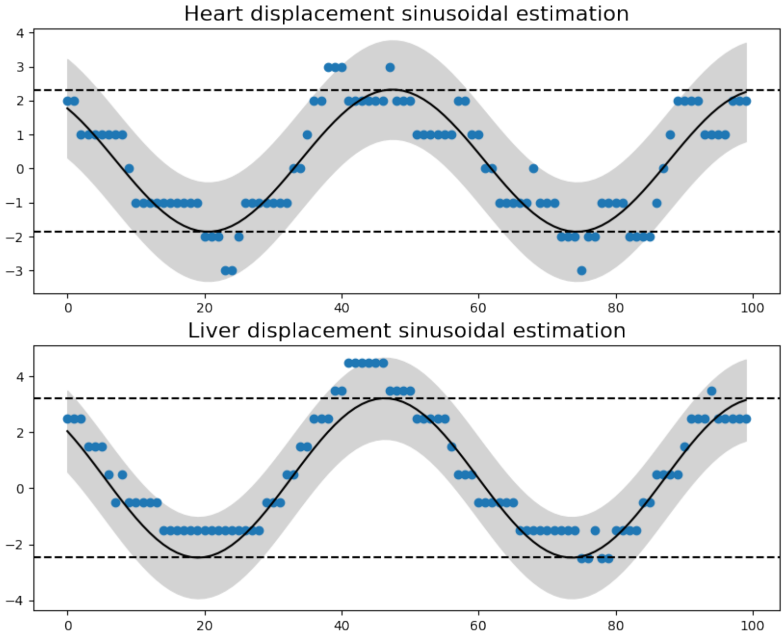

Figure 24: Example sinusoidal curves fit to heart (top) and liver (bottom) displacements. The measured displacements of the heart and liver are shown in blue, with the sinusoidal best fit curve shown in black. One standard deviation in the curve amplitude is shown in gray, and the amplitudes of each fit are indicated by dashed horizontal black lines.

The tracking factor, which provides a measure of the heart's displacement relative to that of the lung-liver interface, was computed using the amplitudes of the sinusoidal fits of the heart and liver displacements. The equation for the relationship is given by :

$$trackingFactor = \frac{amplitude(heart\,displacement\,sine)}{amplitude(liver\,displacement\,sine)} \tag{20}$$

4 Results

4.1 Phantom Testing

4.1.1 Control System Prediction Accuracy

The accuracy of the control system's predictions (red markers in Figure 25) was assessed through comparison with estimates from a best fit line (green in Figure 25) based on past and future navigator measurements (blue in Figure 25).

Both the estimate and the controller predictions are shown alongside the measured displacements in Figure 25.

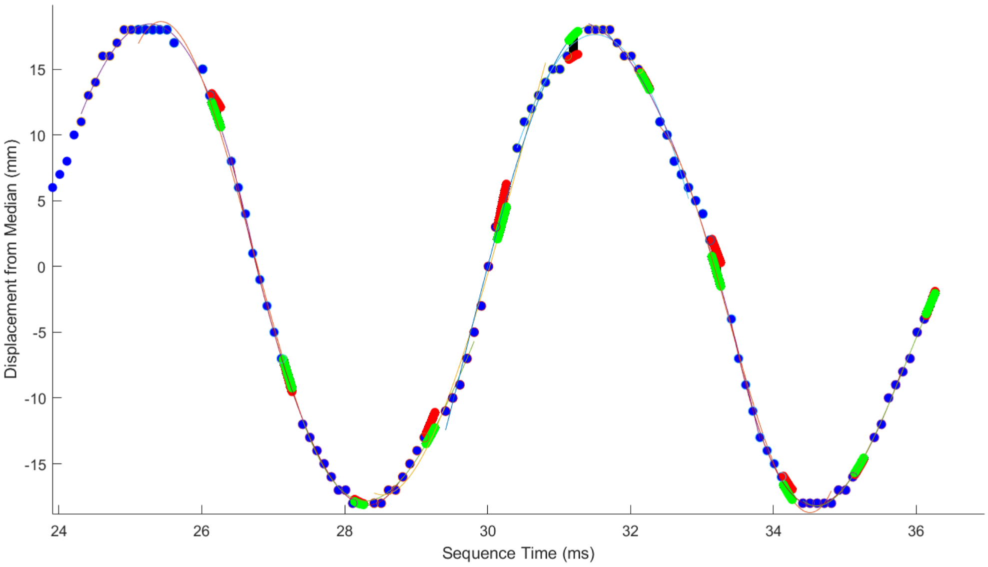

Figure 25: Displacement of the edge of a water phantom when moved in the motion test rig. The blue markers are the navigator measurements of the phantom's displacement (motion); red shows the displacement predicted by the control system during imaging segments (when no navigator readings are available), and green the displacement estimates from a best fit line based on both past and future navigator measurements.

The RMSE for the liquid phantom was calculated to be 1.01±0.93 mm and 1.75±1.02 mm for the pineapple tests.

4.1.2 Image Quality Assessment

The test acquisitions for the liquid phantom are shown in Figure 26.

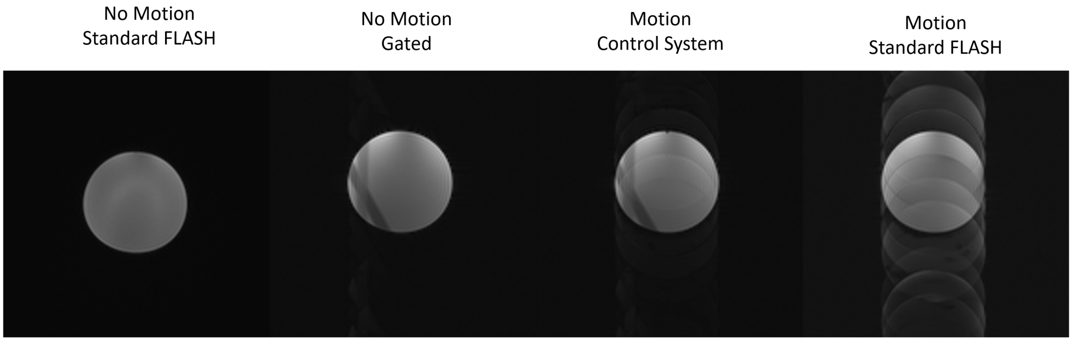

Figure 26: Images acquired from initial liquid phantom tests.

The test acquisitions for the pineapple are shown in Figure 27.

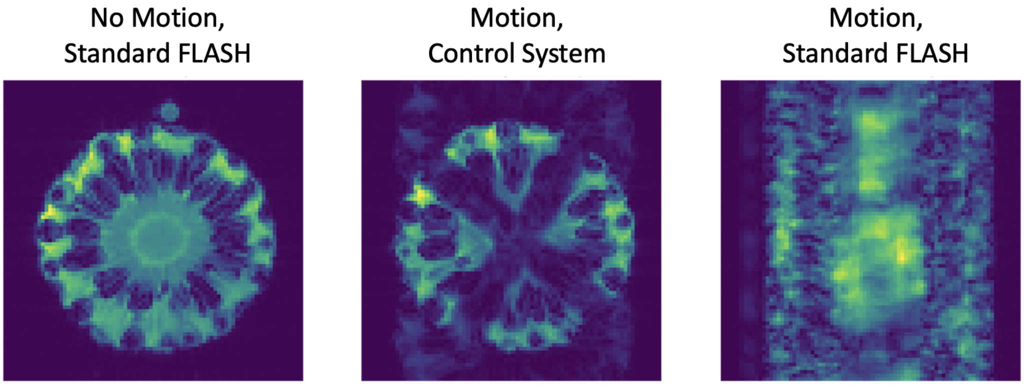

Figure 27: Images acquired from motion correction tests on a pineapple.

The measured two sample pSNR values for the bottle phantom and the pineapple acquisitions are displayed in the bar-charts of Figure 28.

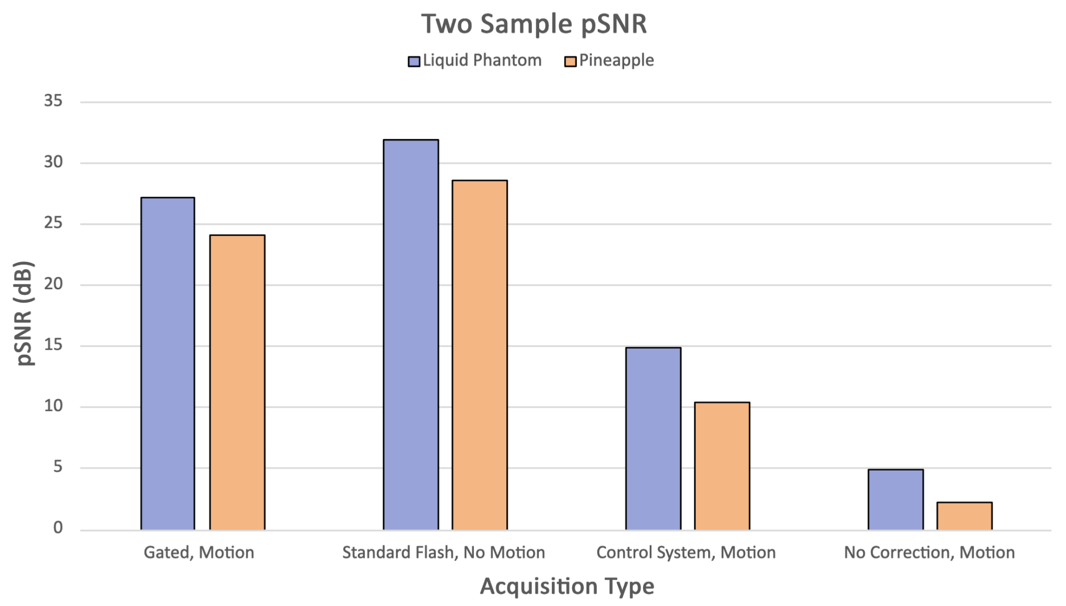

Figure 28: Two sample pSNR results for the liquid phantom (purple) and pineapple (orange) test acquisitions.

4.2 Volunteer Testing

4.2.1 Control System Accuracy

Figure 29 shows the root mean squared errors (RMSEs) of the diaphragm positions predicted by the controller for all the volunteer acquisitions as a function of imaging orientation and tracking factor.

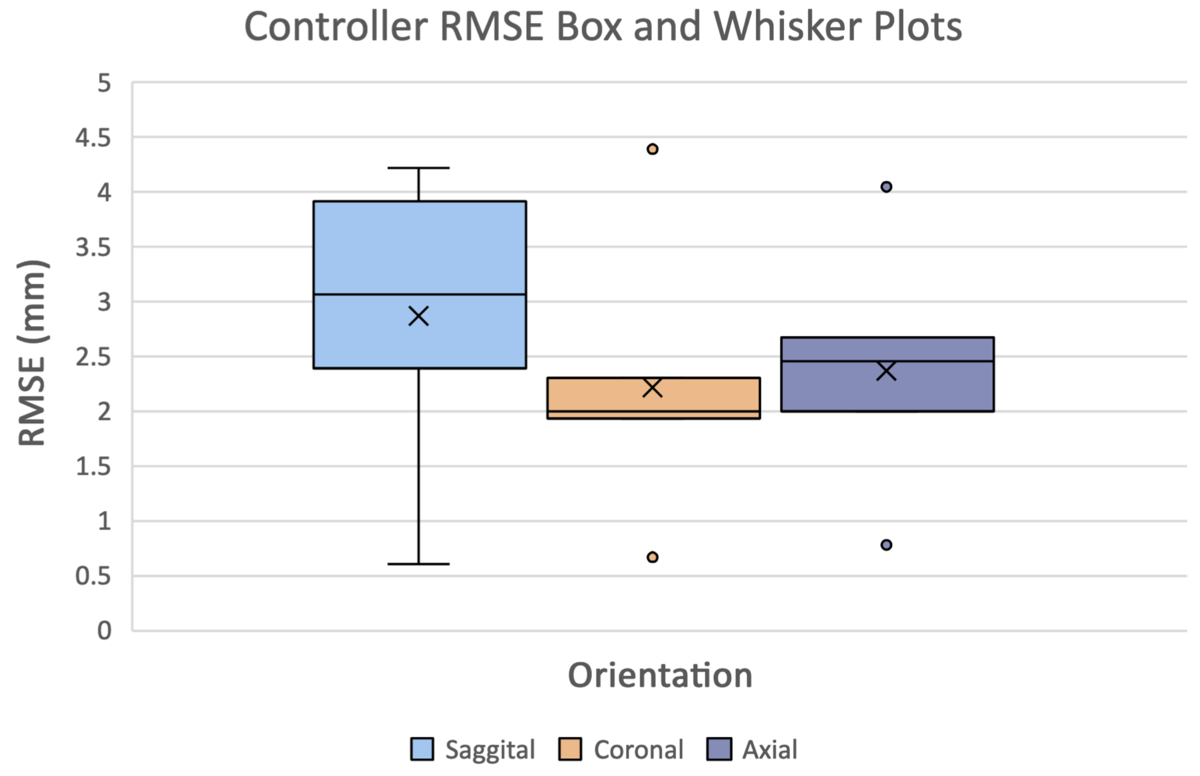

Figure 29: Box and whisker plots of RMSEs of controller the diaphragm positions predicted by the controller. The errors for the sagittal (blue), coronal (orange) and axial (purple) acquisitions. Outliers are shown by points outside of the boxes and whiskers.

4.2.2 Image Quality Assessment

Direct Image Quality Assessment (IQA)

The results of applying direct quality assessment measures (described in table 2) to all of the volunteer acquisitions are shown in the following figures. The box and whisker plots of Figures 30, 31 and 32 display the statistical properties of the results for each measure for the full, cropped and masked images respectively. To aid in analysis, all measures were normalized by scaling down by a constant factor for each measure.

Figure 30: Comparison of image quality measures for gated, control system and free breathing images. (MSE: mean squared error, RMSE: root mean squared error, PSNR: peak signal-to-noise ratio, UQI: universal quality index, SSIM: structural similarity index, ERGAS: Erreur Relative Globale Adimensionnelle de Synthèse, SCC: Structural Correlation Co-efficient, RASE: Relative Average Spectral Error, SAM: Spectral Angle Mapper).

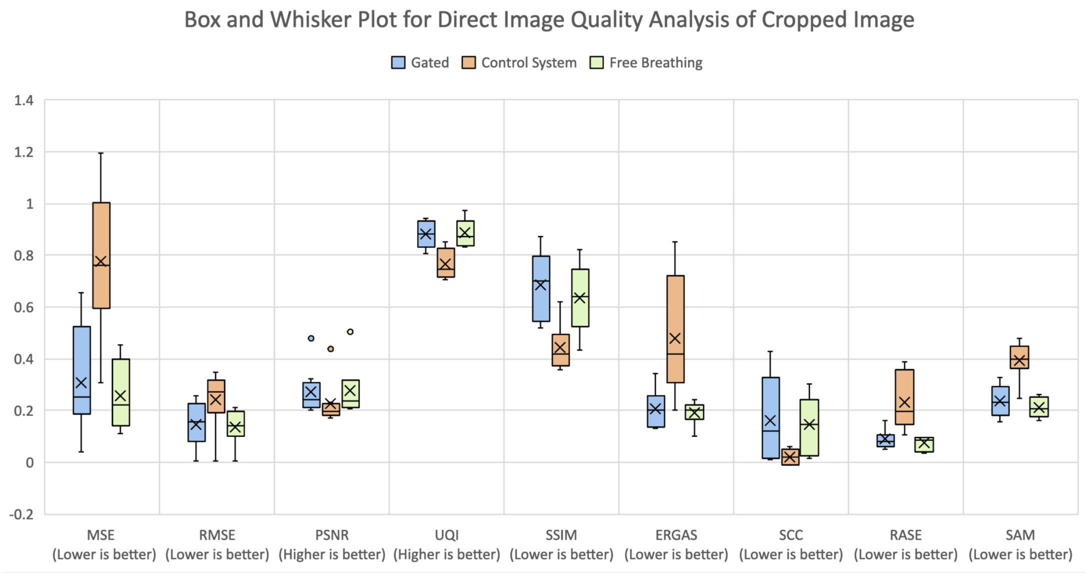

Figure 31: Direct IQA measures applied to all of the cropped volunteer images. MSE: mean squared error, RMSE: root mean squared error, PSNR: peak signal-to-noise ratio, UQI: universal quality index, SSM: structural similarity index, ERGAS: Erreur Relative Globale Adimensionnelle de Synthèse, SCC: Structural Correlation Co-efficient, RASE: Relative Average Spectral Error, SAM: Spectral Angle Mapper).

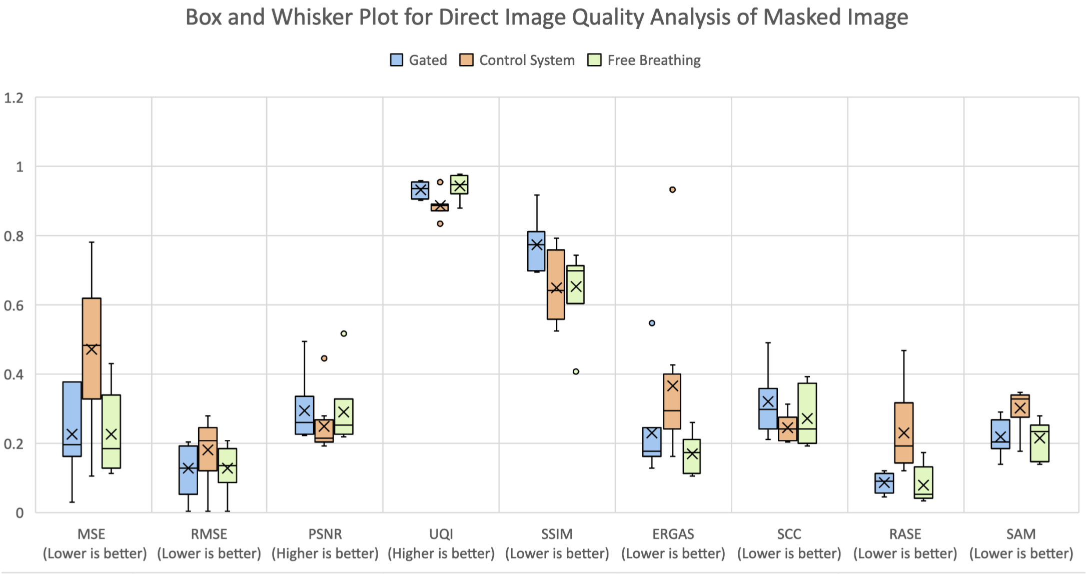

Figure 32: Direct IQA measures applied to all of the masked volunteer images. MSE: mean squared error, RMSE: root mean squared error, PSNR: peak signal-to-noise ratio, UQI: universal quality index, SSM: structural similarity index, ERGAS: Erreur Relative Globale Adimensionnelle de Synthèse, SCC: Structural Correlation Co-efficient, RASE: Relative Average Spectral Error, SAM: Spectral Angle Mapper).

Indirect Quality Assessment

The BRISQUE scores for all of the breath-held, gated, control system and free-breathing images were calculated for the full, cropped and masked volunteer acquisitions. The resulting distributions of the scores for all volunteers are displayed in Figure 33.

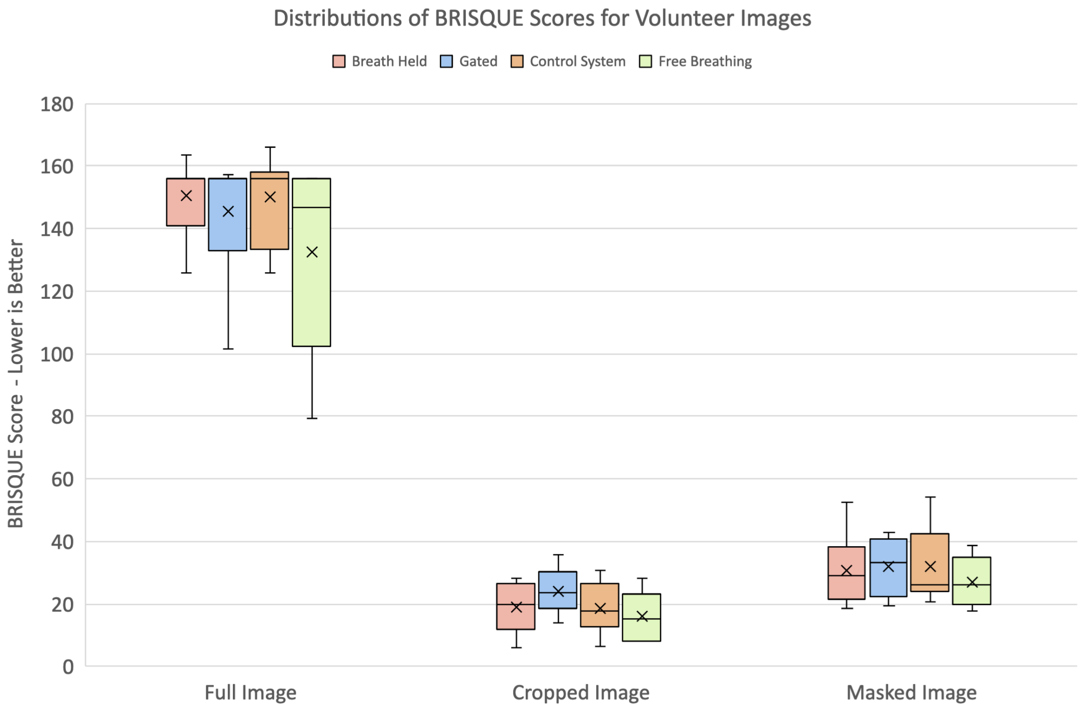

Figure 33: Box and whisker plots of the BRISQUE scores for the full, cropped and masked images. For each set of images the the BRISQUE scores for the breath-held (orange), gated (blue) control system (green) and free breathing (purple) acquisitions are displayed.

Two Sample pSNR Quality Assessment

The two-sample pSNR values for each type of volunteer acquisition is displayed in the box-plots of Figure 34. Note that the pSNR values for each volunteer were normalised by the pSNR of the breath-held acquisition for that volunteer. As such, the pSNR of the breath-held acquisitions are unity, and the pSNR values for all other acquisitions are relative to that.

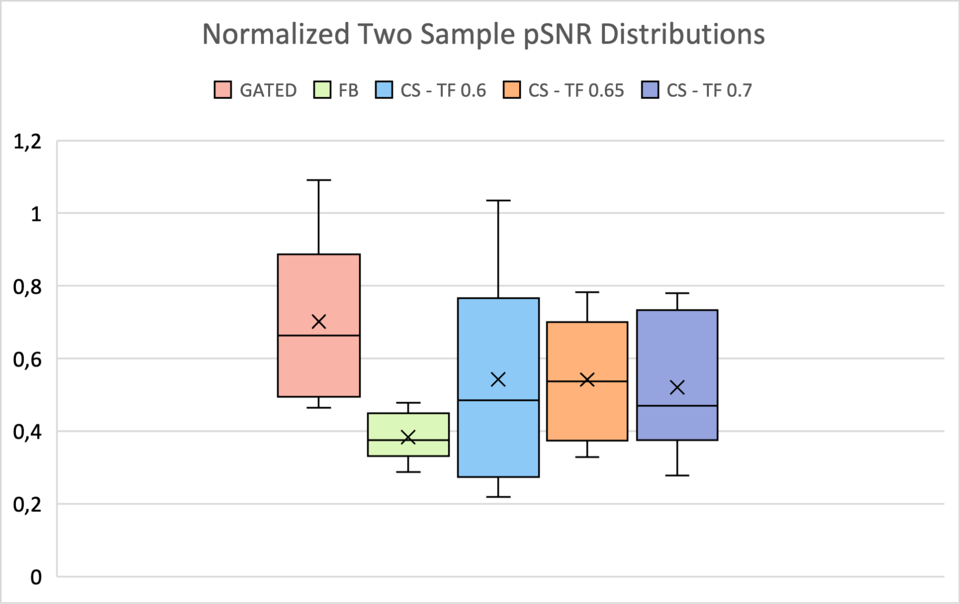

Figure 34: Box and whisker plots of the normalized two sample pSNR results for all volunteer acquisitions. Gated (in red), free-breathing (FB - in green) and control system results for three tracking factor values (0.6 - blue, 0.65 - orange, 0.7 - purple)

Paired t-tests for the pSNR distributions were calculated for the normalised two sample pSNR distributions (Figure 35).

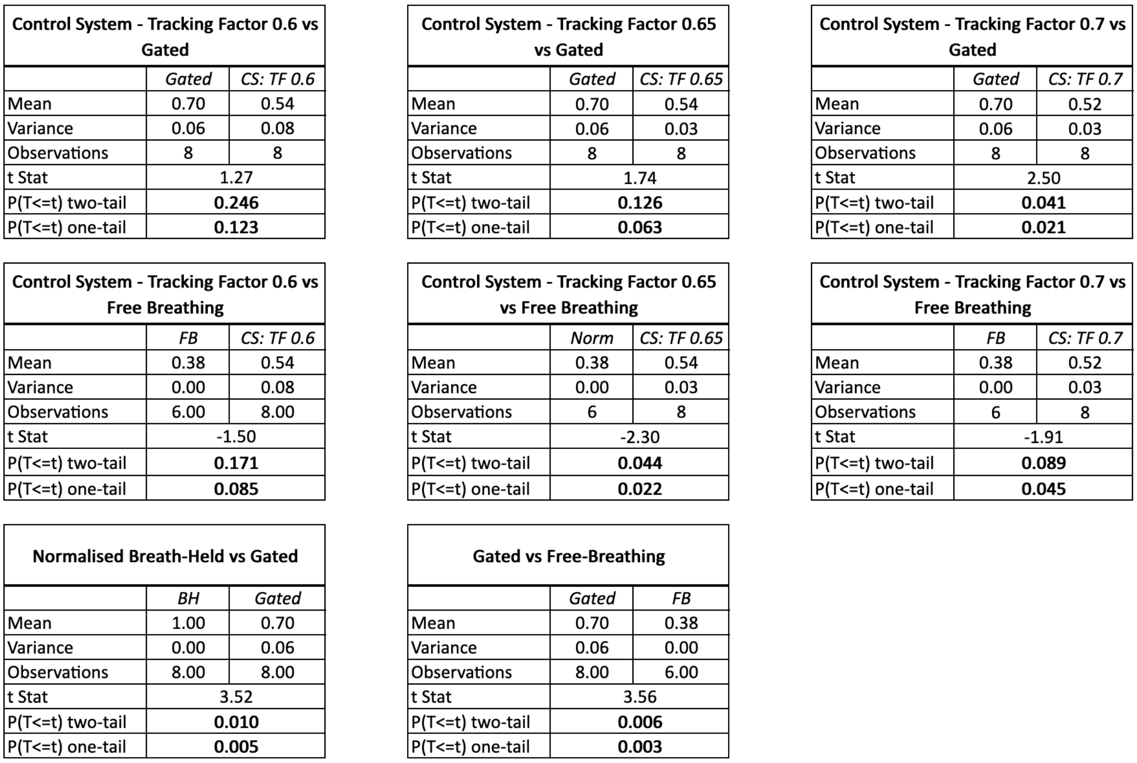

Control System - Tracking Factor 0.6 vs Gated

	Gated	*CS: TF 0.6*
Mean	0.70	0.54
Variance	0.06	0.08
Observations	8	8
t Stat	1.27	
P(T<=t) two-tail	**0.246**	
P(T<=t) one-tail	**0.123**	

Control System - Tracking Factor 0.65 vs Gated

	Gated	*CS: TF 0.65*
Mean	0.70	0.54
Variance	0.06	0.03
Observations	8	8
t Stat	1.74	
P(T<=t) two-tail	**0.126**	
P(T<=t) one-tail	**0.063**	

Control System - Tracking Factor 0.7 vs Gated

	Gated	*CS: TF 0.7*
Mean	0.70	0.52
Variance	0.06	0.03
Observations	8	8
t Stat	2.50	
P(T<=t) two-tail	**0.041**	
P(T<=t) one-tail	**0.021**	

Control System - Tracking Factor 0.6 vs Free Breathing

	FB	*CS: TF 0.6*
Mean	0.38	0.54
Variance	0.00	0.08
Observations	6.00	8.00
t Stat	-1.50	
P(T<=t) two-tail	**0.171**	
P(T<=t) one-tail	**0.085**	

Control System - Tracking Factor 0.65 vs Free Breathing

	Norm	*CS: TF 0.65*
Mean	0.38	0.54
Variance	0.00	0.03
Observations	6	8
t Stat	-2.30	
P(T<=t) two-tail	**0.044**	
P(T<=t) one-tail	**0.022**	

Control System - Tracking Factor 0.7 vs Free Breathing

	FB	*CS: TF 0.7*
Mean	0.38	0.52
Variance	0.00	0.03
Observations	6	8
t Stat	-1.91	
P(T<=t) two-tail	**0.089**	
P(T<=t) one-tail	**0.045**	

Normalised Breath-Held vs Gated

	BH	*Gated*
Mean	1.00	0.70
Variance	0.00	0.06
Observations	8.00	8.00
t Stat	3.52	
P(T<=t) two-tail	**0.010**	
P(T<=t) one-tail	**0.005**	

Gated vs Free-Breathing

	Gated	*FB*
Mean	0.70	0.38
Variance	0.06	0.00
Observations	8.00	6.00
t Stat	3.56	
P(T<=t) two-tail	**0.006**	
P(T<=t) one-tail	**0.003**	

Figure 35: T-test scores for the pSNR distributions. Comparisons for the gated and free breathing acquisitions vs control system acquisitions for all tracking factors are shown. As well as the normalised breath-held, gated and free-breathing acquisitions

4.2.3 Inter-subject Tracking Factor Variability

The tracking factors for each volunteer were calculated from their cine acquisitions, as outlined in Section 3.3.3. The results are listed in Table 3.

Table 3

Calculated Tracking Factors for Volunteers

Volunteer	**2**	**3**	**4**	**5**	**6**	**7**	**8**	**9**
Tracking Factor	0.86	1.02	0.68	0.73	0.58	0.89	0.8	0.75
Standard Deviation	0.12	0.15	0.01	0.01	0.01	0.01	0.03	0.01

5 Discussion

5.1 Simulations

In the simulations, the average of the errors between the controller's predicted positions and the simulated navigator positions were less than a millimeter (see Figure 11). Since the resolution of the navigators used within the FLASH sequence is 1mm, performance of the control system was deemed adequate to proceed with scanner testing.

5.2 Phantom Testing

The images of the liquid phantom acquired with the control system in the presence of motion, shown in Figure 26, still contained substantial motion artifacts. Although the intensity and number of artifacts were noticeably lower than in the uncorrected acquisition, these images do not indicate high quality motion correction. However, the RMSE of 1.01 ± 0.93mm and 1.01 ± 0.93mm, for the phantom and pineapple respectively demonstrates that the controller is able to accurately predict the displacement of the edge of the phantom. Multiple tests were run, without any clear indication of the cause for the observed artifacts.

In comparison to the liquid phantom, the pineapple images acquired with the control system adapted sequence in the presence of motion demonstrate fewer and less prominent artifacts. The cross of lower signal running through the center of the pineapple in the control system acquisition is a result of the cross-pair navigator used for motion tracking. Outside of the navigator saturation areas, the control system acquisition shows internal structures also visible in the static image. This indicates that the controller is able to acquire fine detail whilst compensating for motion.

Despite prospective motion correction, the pSNR values with the control system adapted sequence are, however, roughly half that of the standard acquisition without motion. (Figure 28), as well as that of the gated acquisition with motion, but more than three times higher than an acquisition with motion but without any motion correction.

5.3 Volunteer Testing

5.3.1 Controller Accuracy

In development of a prospective motion correction cardiac MRI sequence Bush et al. (2019) reported an RMSE of 0.61mm with a range of 3.27mm, resulting in a tracking error within the 4mm gated sequence window. These ranges are useful in framing the results of the control system's accuracy. As shown in Figure 29, the mean of the RMSEs for all orientations and all tracking factors were below 3.5mm, with most means below 3mm.

In some cases, such as volunteer 3, the controller predictions demonstrated sub-millimeter accuracy; the mean RMSEs were 0.66 ± 0.16mm, 0.51 ± 0.08mm and 0.86 ± 0.07mm across all orientations. The accuracy is likely due to the very regular and sinusoidal breathing pattern of volunteer 3 both during the initial scout readings used to train the model, and throughout all of the imaging segments. A sample of the recorded navigator positions and the control system predictions acquired during imaging of volunteer 3 is shown in Figure 36. Notably, the largest tracking factor errors in Figure 36 occur in the non-linear regions of the breathing pattern. This is expected, as the controller is effectively using a linear approximation of the breathing model, and data are linearly interpolated for computational efficiency. It is important to also note that one of the key limiting factors of the controller's accuracy is the data from the navigators themselves. Since the navigator resolution is 1mm, the sub-millimeter motion will be rounded up or down to the nearest millimeter, providing flat lines as seen in Figure 36. These flat sections can mislead the controller predictions during the imaging segment.

However, most volunteer breathing patterns were observed to not be as sinusoidal in shape as modeled as seen in Volunteer 3. Some volunteers exhibited periods of little to no motion, followed by deep exhalation, indicating ”sighs” present in most natural breathing (Ramirez, 2014). An example of this can be seen in Figure 37.

As expected, this breathing pattern has a negative impact on the controller's ability to track motion accurately. This can be seen in Figure 38. Of particular note are the third imaging segment (indicated by a red arrow) and the imaging segments leading into the second peak (indicated by a red circle). In the case of the third imaging segment, the controller behaves well according to the navigator's data prior to the imaging segment. However, the navigator data preceding the imaging segment incorrectly show a plateau

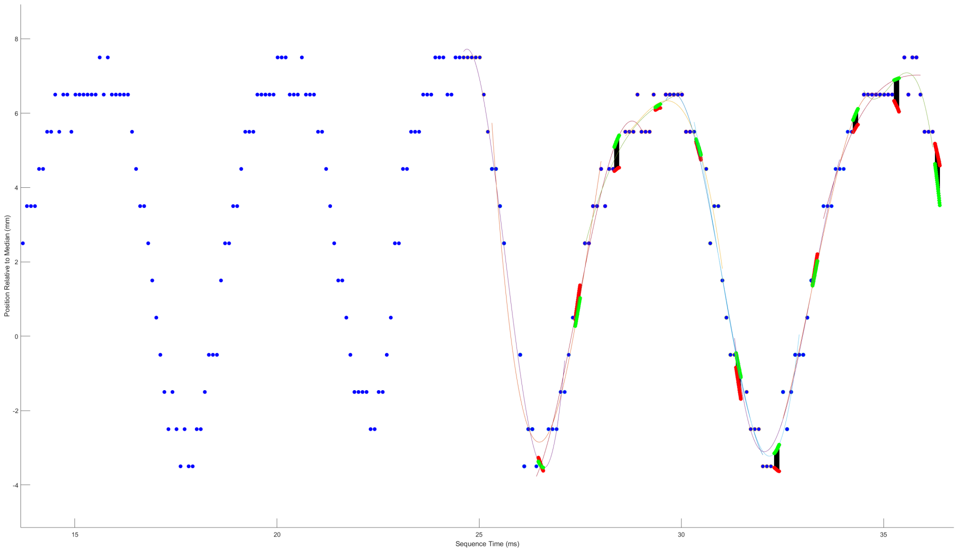

Figure 36: Plot of the recorded navigator positions (blue), predicted controller positions (red), best fit lines (multi-colored) and best fit positions (green), acquired whilst imaging volunteer 3.

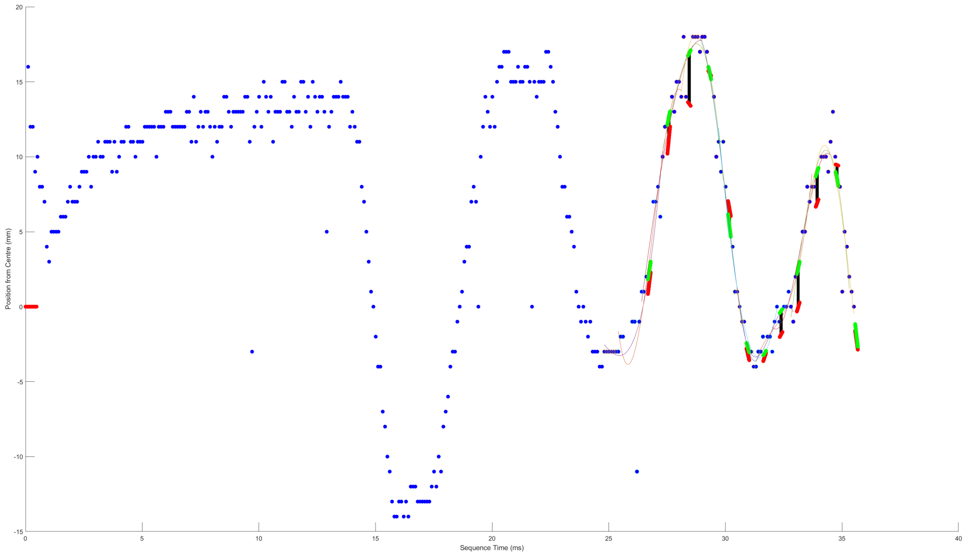

Figure 37: Plot indicating non-sinusoidal breathing patterns during initial training of the control system before imaging.

in the breathing motion, whereas subsequent navigator positions correspond to the true peak. In the case of the imaging segments leading into the second peak, the controller's displacement predictions are accurate in moving with the peak, but are consistently less than the estimates from the best fit line using past and future navigator readings. These errors were most likely caused by the irregular breathing pattern data recorded during the initial scout navigators. Although the controller is not completely dependent on accurate scout readings, as the breathing of the subject is continuously tracked, it will be negatively affected by irregular training data.

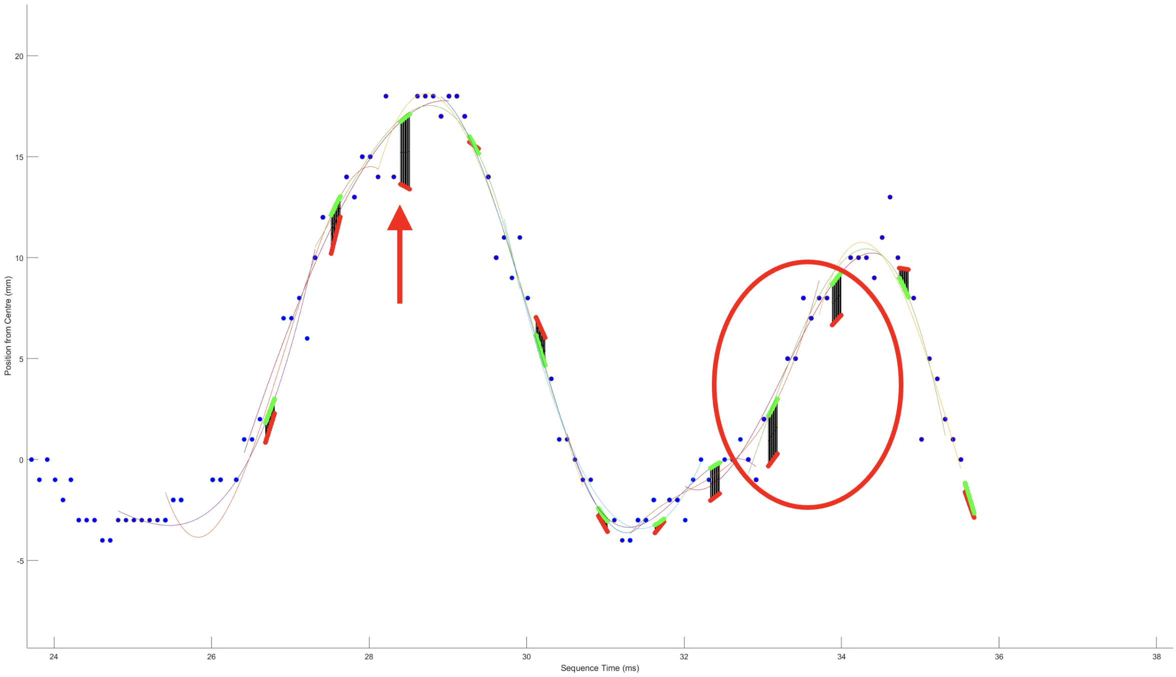

Figure 38: Subsection Plot of Figure 37 Indicating Controller-System Error During the Imaging Segments. Red arrow: inaccurate navigator plateau misleading controller predictions. Red circle: controller predictions below navigator positions due to noisy readings at the trough.

The most damaging effect to the controller's accuracy over the entire scan results from inaccurate calculation of the subject's median breathing position. An example of the negative effect is shown in Figure 39.

Although the controller is accurately predicting the displacements during the imaging segments, they are all shifted down by a constant factor. This is the most notable negative impact as all positions in all imaging segments across the entire acquisition are affected. In this case the error cannot be corrected between imaging segments and thus negates the benefits of the control system's feedback loop.

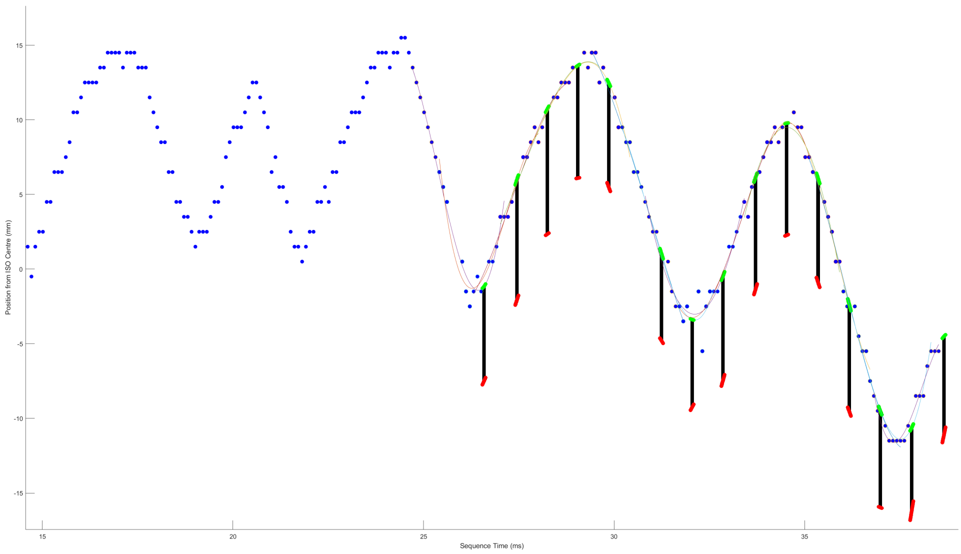

Figure 39: Plot showing the effect of incorrect median calculation on the control system's predicted positions during the imaging segment

5.3.2 Image Quality Assessments

Direct Analysis

Since images acquired without correction whilst breathing freely demonstrated more severe and a greater number of artifacts than images acquired using any other techniques (breath-held, gated or control system), we expected the image quality metrics from these uncorrected free breathing acquisitions to reflect the poorest image quality. However, within the full image analyses, most of the direct quality measures suggest that the uncorrected free-breathing acquisitions performed better than the gated acquisitions (Figure 30). The exceptions were the UQI, ERGAS and RASE measures.

After cropping (Figure 31) and masking (Figure 32) the images to include only the heart, the results were worse. Now all the image quality metrics were better or similar for the uncorrected free-breathing images than those acquired using standard gating techniques. The inaccuracy of these results in capturing the poor image quality of the uncorrected free-breathing images highlight that direct image quality assessments are not able to provide a valid assessment of the image quality in this setting. These measures were therefore not considered further in the study.

Indirect Analysis

In contrast to the direct image quality measures, BRISQUE scores (Figure 33) suggest similar image quality for breath-held, standard gated, control system, and free-breathing acquisitions. Notably, the BRISQUE scores of all the acquisitions are substantially improved by cropping and masking the images to only include the heart region

While these results are closer to the truth, it is still not aligned with the substantial degradation and poor image quality seen in the images from the uncorrected free-breathing acquisitions. It is evident from visual inspection that significantly more structure and fewer artifacts are present in the breath-held acquisitions. Therefore the BRISQUE analysis also does not provide a useful quality assessment metric within this study and cannot be used to quantify the quality of the control-system adapted acquisitions.

5.3.3 Two Sample pSNR

In contrast to the direct and indirect IQA measures, the two sample pSNR measure produced a consistent result, wherein scores from the breath-held and gated acquisitions were better on average than for uncorrected free-breathing acquisitions. In addition, gated acquisitions produced lower pSNR values than breath-held, as expected. This suggests that the two-sample pSNR test can be considered a useful measure of image quality, when comparing the various acquisitions.

In all of the volunteers the quality was the highest for the standard breath-held acquisitions, which were used as reference for normalisation of pSNR scores in Figure 34. The gated acquisitions introduced a drop in the quality compared to the normalised breath-held scores, (one-tailed paired t-test, $p = 0.005$) and did not always remove respiratory motion artifacts.

The pSNR scores for acquistions with the control system were similar to those of the gated acquisition, except for the control system acquisitions with a tracking factor of 0.7, for which the pSNR scores were about 26% lower than for the gated acquisitions (one tailed paired t-test, p=0.02). In contrast, the quality of the pSNR scores of the free-breathing acquisitions were lower than for the control system acquisitions with the tracking factors 0.65 and 0.7 (one tailed paired t-test, p's ¡0.05), and lower than for gated acquisitions (p=0.003). While these results support that the quality of images obtained using the control system are comparable to those from gated acquisitions and better than free-breathing, it is evident that the inter-subject tracking factor variability impacts image quality.

However, some results from the control system adapted sequence that highlight that when the system works well, it can provide quality equal to, and sometimes beyond, gated acquisitions.

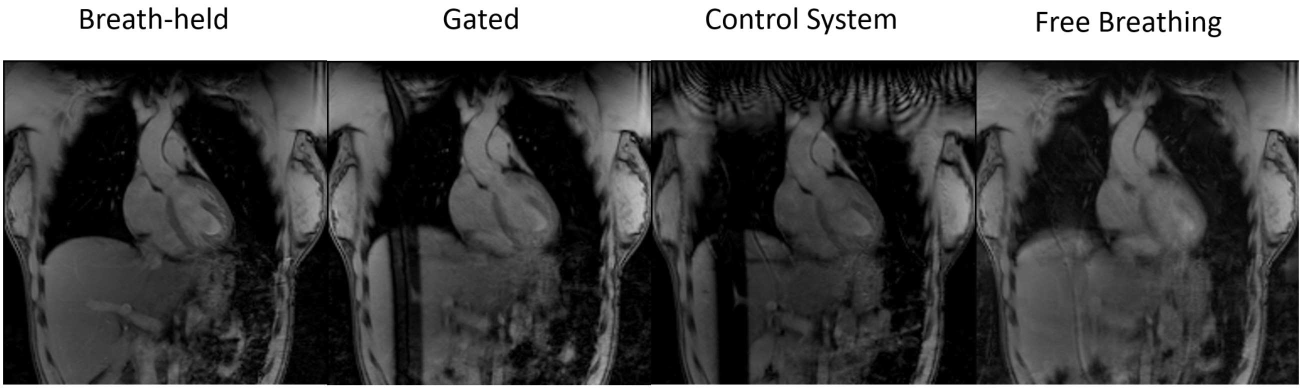

Figure 40: Sample coronal images of volunteer 7 from breath-held, gated, control system and free-breathing sequences

Figure 40 shows images acquired for volunteer 7 in the coronal plane with each of the techniques. In this instance, the two sample analysis yields similar pSNR values for the standard gated and control system acquisitions. Although the control system acquisitions is more susceptible to Moiré fringes (see also Figure 41), there is good contrast and definition in the heart region. Notably the control system's image is clearer than the free breathing acquisition with no correction.

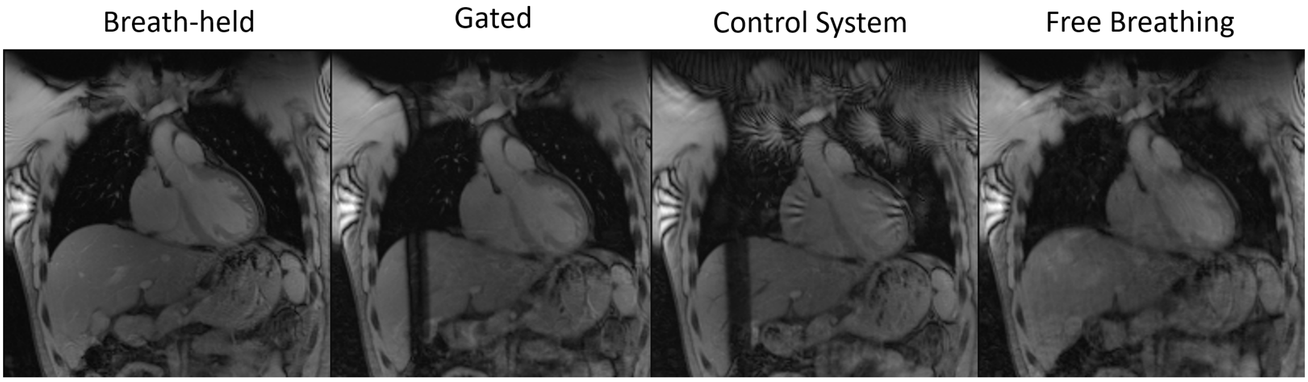

Figure 41: Sample coronal images of volunteer 8 from breath-held, gated, control system and free-breathing sequences

Whilst the controller's accuracy was an important factor in determining the efficacy of the slice following, and the resulting image quality, accurate slice following did not guarantee good image quality. An example of this is seen for volunteer 3 (Figure 42). Despite the fact that motion was tracked accurately for this volunter (RMSE's ¡ 1mm), the quality of the control system images were lower than for the gated acquisition's. Moreover, the control system images for volunteer 3 were impacted substantially by Moiré fringes. Although it is possible to find regions of high contrast and clear edge clarity within the image, it would not be possible to consider this image of a similar quality as the breath-held and gated acquisition.

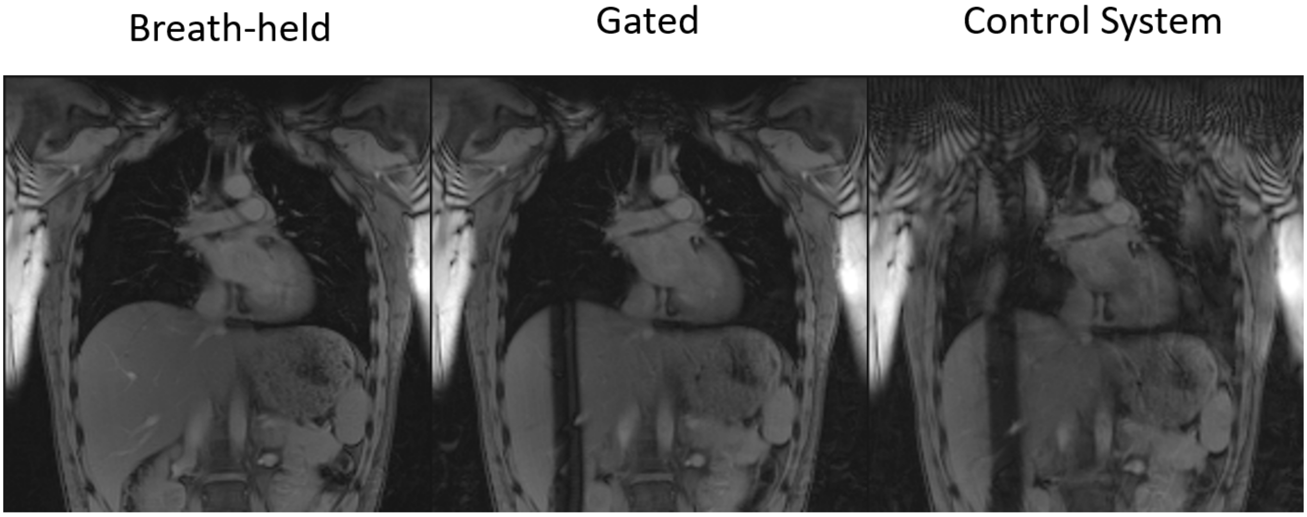

Breath-held

Gated

Control System

Figure 42: Sample coronal images of volunteer 3 from breath-held, gated and control system sequences.

These results all indicate that further investigation into the phase encoding interference is required in order to produce a robust and viable implementation of the control system sequence. An investigation into the effect of phase encoding was carried out during experimentation. The phase encoding direction was flipped in some volunteers in order to determine if the resulting interference patterns were reduced or removed.

Comparison of the images in Figure 43 acquired with different phase encode directions, indicate that while the phase encode direction affects the interference, it does not necessarily increase or decrease the amount of interference.

Another important factor affecting the quality of both the gated and control system images is the orientation of the image. Both navigated sequences provided higher quality results in the coronal plane, and were more prone to respiratory motion artifacts in the axial and sagittal planes. The axial images for volunteer 8 are shown in Figure 44. It is clear that both the control system and the gated acquisitions both suffer from motion artifacts due to the expansion and compression of the chest wall during imaging.

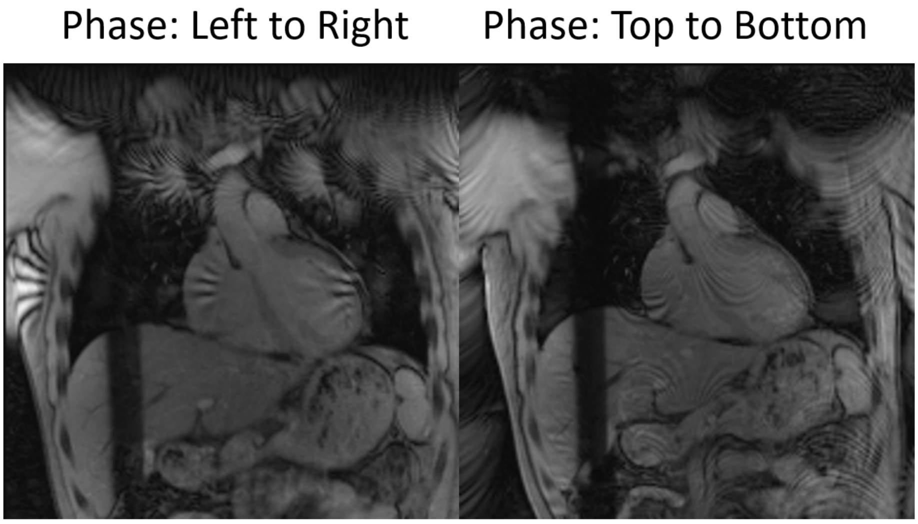

Figure 43: Two coronal control system image of volunteer 8 with differing phase encoding directions.

Whilst all results are still less noisy than the free-breathing acquisition, the breath-held acquisition is the only technique that provided a clear image without artifacts.

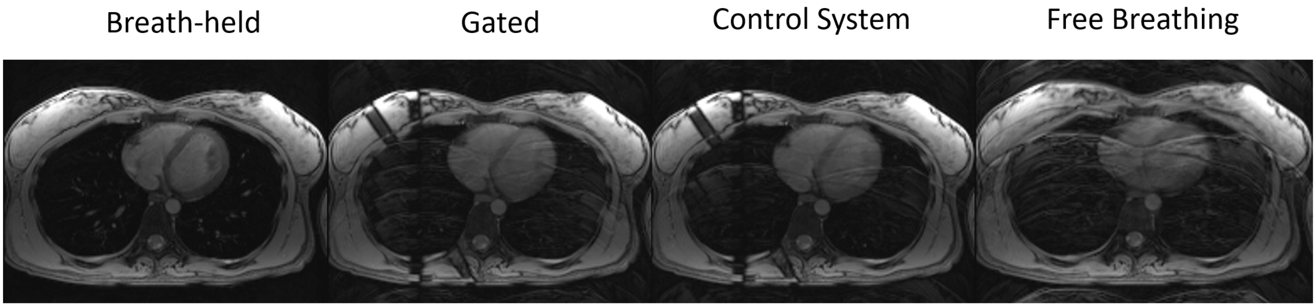

Figure 44: Sample axial images of volunteer 8 from breath-held, gated, control system sequences and free-breathing sequences.

Similarly, acquisitions in the sagittal plane contain artifacts for both the gated and control system sequences. These artifacts are shown below in Figure 45.

The compensation for the non-linear motion of the chest during respiration therefore remain a challenge for navigated slice following sequences.

Limitations of Two Sample pSNR Analysis

The heart region selected for our pSNR analysis is a limitation in the current study. Typically, in clinical diagnosis, only sections of the heart comprising uniform tissue (for example , the myocardium or the septum) would be selected. However, this study has

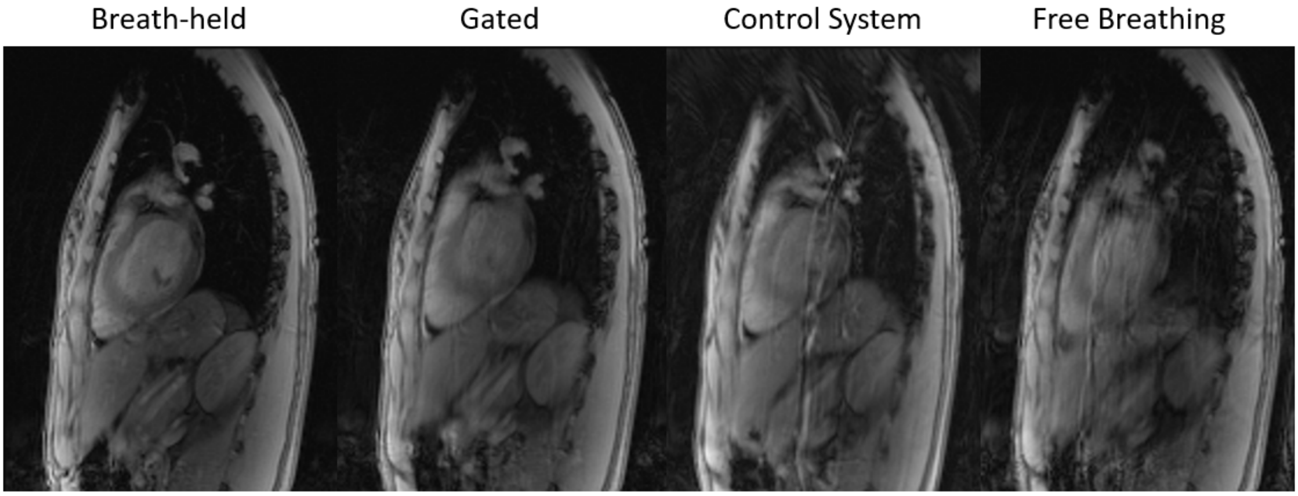

Figure 45: Sample sagittal images of volunteer 7 from breath-held, gated, control system sequences and free-breathing sequences.

computed an average pSNR over the entire heart. Therefore, it is likely, such as in the case of volunteer 8 (Figure 41), that the pSNR score for the useful septum region might result in a higher pSNR score than was reported for the entire heart. Future studies aiming to improve the performance of the control system should instead perform detailed sub-region analyses.

5.3.4 Inter-subject Tracking Factor Variability

The linear tracking factors that define the displacement of the heart relative to that of the diaphragm, were found to be highly variable amongst the volunteers and ranged from 0.68 to 1.02. However, within each volunteer the tracking factors were highly consistent throughout the entire breathing cycle, when measured in the coronal orientation (standard deviations for volunteer 6 and 8 of < 0.04). The widely accepted estimate reported as a best-fit for every person, of 0.6 (Y. Wang et al., 1995), would therefore, result in substantial errors when following the heart based on diaphragm positions. These results suggest that preforming a pre-scan to compute subject-specific tracking factors may significantly improve slice following accuracy in free breathing cardiac MRI.

6 Conclusion

6.1 Conclusions

A motion corrected FLASH sequence utilizing an observer predictor controller for real-time slice following was successfully developed, implemented and tested, both in phantoms and in nine healthy volunteers. On phantom tests, the RMSEs of the controller's predictions during the imaging segments were ¡2mm. In free-breathing human volunteers, the mean RMSE of the predicted diaphragm position was 2.64mm. Notably, the accuracy was greater in axial and coronal imaging than in axial.

Both direct and indirect image quality assessment metrics were shown to be inappropriate to assess image quality in this context. In contrast, two sample pSNR measures demonstrate similar image quality for control system and gated acquisitions, except for those using a tracking factor of 0.7. Although the resulting control system acquisitions were not reliably free of motion artifacts, the sequence was able to provide quality similar to and sometimes better then the corresponding gated acquisitions in specific acquisitions. Overall, the control system sequence was reliably better in image quality than the uncorrected free-breathing acquisitions when using a tracking factor of 0.65.

The study results clearly show that there is a large amount of variation in the linear factor which relates volunteer diaphragm positions with heart positions. The subject specific nature of this factor will consistently have a negative effect on any prospective motion correction system's accuracy and therefore must be considered by similar diaphragm tracking techniques.

6.2 Future Recommendations

Whilst the control system's predictions of diaphragm positions are accurate, there are a number of improvements that could ensure more robust tracking. The navigators used for tracking the diaphragm positions outside of the imaging segment are crucial for calculating the error of the control system's feedback loop and updating future predictions. Because of this, these predictions are hampered by the current 1mm resolution of the navigators. The navigator positions frequently provided long periods of ”flat” position readings when the movement would be sub-millimeter, incorrectly indicating that the diaphragm is at rest. Furthermore noise in the navigator readings impacts predictions negatively. Improving both of these aspects would ensure more accurate diaphragm position predictions with the control system adapted sequence. A more effective low-pass filter should be applied to the navigator readings and a finer sub-millimeter navigator utilized, if available.

Alongside these, improvements to the training of the controller could lower its susceptibility to outlier noise and irregular breathing during the initial 256 scout readings. Further research should also be considered on the impact of volunteer breathing patterns. Tests where the volunteer is encouraged to breathe deeply or shallowly could provide important information on how to improve the motion correction. All improvements to the controller's accuracy will be negated if the linear factor between the diaphragm position and the heart's position are inaccurate for the particular subject. As such, it is important to explore options for calculating subject specific tracking factors. Ideally this would be implemented within the initial 256 training scouts at the start of the sequence.

An aspect for improvement separate from the control system is the Moiré interference artifacts. Further research is needed to identify the root cause of the field inhomogeneities which are the main cause of Moiré interference. It is possible that this is a more fundamental imaging concern, caused due to the motion of the thoracic organs relative to the body coil. Another fundamental challenge that will require addressing is motion present due to the expansion and contraction of the chest.

References

A.C. Bovik, Zhou Wang, & H.R. Sheikh. (2004). Image quality assessment: From error visibility to structural similarity — IEEE Journals & Magazine — IEEE Xplore.

Bradski, G. (2000). The OpenCV Library. *Dr. Dobb's Journal of Software Tools*.

Burger, I. (2012). A control system approach to subject specific prospective respiratory motion correction in cardiac MRI, 98.

Burger, I., & Meintjes, E. M. (2013). Elliptical subject-specific model of respiratory motion for cardiac MRI: Elliptical Subject-Specific Model. *Magnetic Resonance in Medicine*, *70*(3), 722–731. https://doi.org/10.1002/mrm.24502

Bush, M. A., Ahmad, R., Jin, N., Liu, Y., & Simonetti, O. P. (2019). Patient specific prospective respiratory motion correction for efficient, free-breathing cardiovascular MRI. *Magnetic Resonance in Medicine*, *81*(6), 3662–3674. https://doi.org/10.1002/mrm.27681

Crum, W. R., Hartkens, T., & Hill, D. L. G. (2004). Non-rigid image registration: Theory and practice. *The British Journal of Radiology*, *77*(suppl_2), S140–S153. https://doi.org/10.1259/bjr/25329214

Danias, P. G., McConnell, M. V., Khasgiwala, V. C., Chuang, M. L., Edelman, R. R., & Manning, W. J. (1997). Prospective navigator correction of image position for coronary MR angiography. *Radiology*, *203*(3), 733–736. https://doi.org/10.1148/radiology.203.3.9169696

Dey, J., Segars, W. P., Pretorius, P. H., Walvick, R. P., Bruyant, P. P., Dahlberg, S., & King, M. A. (2010). Estimation and correction of cardiac respiratory motion in SPECT in the presence of limited-angle effects due to irregular respiration. *Medical Physics*, *37*(12), 6453–6465. https://doi.org/10.1118/1.3517836

Dietrich, O., Raya, J., Reeder, S., Reiser, M., & Schoenberg, S. (2007). Measurement of signal-to-noise ratios in MR images: Influence of multichannel coils, parallel imaging, and reconstruction filters. *Journal of Magnetic Resonance Imaging*, *26*, 375–85. https://doi.org/10.1002/jmri.20969

Ehman, R. L., & Felmlee, J. P. (1989). Adaptive technique for high-definition MR imaging of moving structures. *Radiology*, *173*(1), 255–263. https://doi.org/10.1148/radiology.173.1.2781017

Gonzalez-Audicana, M., Saleta, J., Catalan, R., & Garcia, R. (2004). Fusion of multispectral and panchromatic images using improved IHS and PCA mergers based on wavelet decomposition. *IEEE Transactions on Geoscience and Remote Sensing*, *42*(6), 1291–1299. https://doi.org/10.1109/TGRS.2004.825593

Haase, A., Frahm, J., Matthaei, D., Hanicke, W., & Merboldt, K. .-. (1986). FLASH imaging. Rapid NMR imaging using low flip-angle pulses. *Journal of Magnetic*

Resonance (1969), *67*(2), 258–266. https://doi.org/10.1016/0022-2364(86)90433-6

Hardy, C. J., Saranathan, M., Zhu, Y., & Darrow, R. D. (2000). Coronary angiography by real-time MRI with adaptive averaging, 7.

Higgins, C. B., Byrd, B. F., McNamara, M. T., Lanzer, P., Lipton, M. J., Botvinick, E., Schiller, N. B., Crooks, L. E., & Kaufman, L. (1985). Magnetic resonance imaging of the heart: A review of the experience in 172 subjects. *Radiology*, *155*(3), 671–679. https://doi.org/10.1148/radiology.155.3.3159039

Jhooti, P., Keegan, J., & Firmin, D. N. (2010). A fully automatic and highly efficient navigator gating technique for high-resolution free-breathing acquisitions: Continuously adaptive windowing strategy: ContinuousLy Adaptive Windowing Strategy (CLAWS). *Magnetic Resonance in Medicine*, *64*(4), 1015–1026. https://doi.org/10.1002/mrm.22491

Kuruppu, S. S., & Shibilski, A. (2019). Clock Variation Impact on Digital Control System Performance. *2019 IEEE 10th Annual Ubiquitous Computing, Electronics Mobile Communication Conference (UEMCON)*, 0353–0358. https://doi.org/10.1109/UEMCON47517.2019.8992979

Küstner, T., Armanious, K., Yang, J., Yang, B., Schick, F., & Gatidis, S. (2019). Retrospective correction of motion-affected MR images using deep learning frameworks. *Magnetic Resonance in Medicine*, *82*(4), 1527–1540. https://doi.org/10.1002/mrm.27783

Ledesma-Carbayo, M. J., Kellman, P., Hsu, L.-Y., Arai, A. E., & McVeigh, E. R. (2007). Motion corrected free-breathing delayed-enhancement imaging of myocardial infarction using nonrigid registration. *Journal of magnetic resonance imaging: JMRI*, *26*(1), 184–190. https://doi.org/10.1002/jmri.20957

Maluleke, R. (2016). Mortality and causes of death in South Africa, 2016: Findings from death notification.

McConnell, M. V., Khasgiwala, V. C., Savord, B. J., Chen, M. H., Chuang, M. L., Edelman, R. R., & Manning, W. J. (1997). Prospective adaptive navigator correction for breath-hold MR coronary angiography. *Magnetic Resonance in Medicine*, *37*(1), 148–152. https://doi.org/10.1002/mrm.1910370121

Mehena, J. (2013). Medical Images Edge Detection Based on Mathematical Morphology. *International Journal of Computer and Communication Technology*, 7–11. https://doi.org/10.47893/IJCCT.2013.1162

Pauli Virtanen, Ralf Gommers, et. al. (2020). SciPy 1.0: Fundamental Algorithms for Scientific Computing in Python. *Nature Methods*, *17*(3), 261–272.

Powell, J., & Franklin, G. (1998). *Digital control of dynamic systems*. Addison-Wesley.

Ramirez, J.-M. (2014). The Integrative Role of the Sigh in Psychology, Physiology, Pathology, and Neurobiology. *Progress in brain research*, *209*, 91–129. https://doi.org/10.1016/B978-0-444-63274-6.00006-0

Robert Fisher, Simon Perkins, Ashley Walker, & Erik Wolfart. (2003). The HIPR Copyright.

Rosslyn. (2001). Determination of signal-to-noise ratio (SNR) in diagnostic magnetic resonance imaging. *NEMA Standards Publication MS 1-2001.*, 15.

Roth, G. A., Abate, D., Abate, K. H., Abay, S. M., Abbafati, C., Abbasi, N., Abbastabar, H., Abd-Allah, F., Abdela, J., Abdelalim, A., Abdollahpour, I., Abdulkader, R. S., Abebe, H. T., Abebe, M., Abebe, Z., Abejie, A. N., Abera, S. F., Abil, O. Z., Abraha, H. N., … Murray, C. J. L. (2018). Global, regional, and national age-sex-specific mortality for 282 causes of death in 195 countries and territories, 1980–2017: A systematic analysis for the Global Burden of Disease Study 2017. *The Lancet*, *392*(10159), 1736–1788. https://doi.org/10.1016/S0140-6736(18)32203-7

Scott, A. D., Keegan, J., & Firmin, D. N. (2009). Motion in Cardiovascular MR Imaging. *Radiology*, *250*(2), 331–351. https://doi.org/10.1148/radiol.2502071998

Sheikh, H., & Bovik, A. (2006). Image information and visual quality. *IEEE Transactions on Image Processing*, *15*(2), 430–444. https://doi.org/10.1109/TIP.2005.859378

Taylor, A. M., Keegan, J., Jhooti, P., Firmin, D. N., & Pennell, D. J. (1999). Calculation of a subject-specific adaptive motion-correction factor for improved real-time navigator echo-gated magnetic resonance coronary angiography. *Journal of Cardiovascular Magnetic Resonance: Official Journal of the Society for Cardiovascular Magnetic Resonance*, *1*(2), 131–138. https://doi.org/10.3109/10976649909080841

Wald, L. (2000). Quality of high resolution synthesised images: Is there a simple criterion ? *Third Conference "Fusion of Earth Data: Merging Point Measurements, Raster Maps and Remotely Sensed Images"*, 99.

Wang, Y., Riederer, S. J., & Ehman, R. L. (1995). Respiratory Motion of the Heart: Kinematics and the Implications for the Spatial Resolution in Coronary Imaging. *Magnetic Resonance in Medicine*, *33*(5), 713–719. https://doi.org/10.1002/mrm.1910330517

_eprint: https://onlinelibrary.wiley.com/doi/pdf/10.1002/mrm.1910330517

Wang, Z., & Bovik, A. (2002). A universal image quality index. *IEEE Signal Processing Letters*, *9*(3), 81–84. https://doi.org/10.1109/97.995823

Yu, S., Dai, G., Wang, Z., Li, L., Wei, X., & Xie, Y. (2018). A consistency evaluation of signal-to-noise ratio in the quality assessment of human brain magnetic resonance images. *BMC Medical Imaging*, *18*(1), 17. https://doi.org/10.1186/s12880-018-0256-6

Yuhas, R. H., Goetz, A. F. H., & Boardman, J. W. (1992). Discrimination among semi-arid landscape endmembers using the Spectral Angle Mapper (SAM) algorithm
NTRS Author Affiliations: Colorado Univ., Commonwealth Scientific and Industrial Research Organization NTRS Document ID: 19940012238 NTRS Research Center: Legacy CDMS (CDMS).

Zhou, J., Civco, D. L., & Silander, J. A. (1998). A wavelet transform method to merge Landsat TM and SPOT panchromatic data. *International Journal of Remote Sensing*, *19*(4), 743–757. https://doi.org/10.1080/014311698215973
_eprint: https://doi.org/10.1080/014311698215973

7 Appendix A - Table Data

Controller RMSE Data

	Volunteer 3			**Volunteer 4**			**Volunteer 5**			**Volunteer 6**		
	TF 0.6	**TF 0.65**	**TF 0.7**	**TF 0.6**	**TF 0.65**	**TF 0.7**	**TF 0.6**	**TF 0.65**	**TF 0.7**	**TF 0.6**	**TF 0.65**	**TF 0.7**
sag	0.4819	0.4199	0.8865	2.9435	2.8574	3.4673	2.1494	2.2084	11.1793	2.7111	2.3187	3.5369
cor	0.6138	0.6043	0.758	3.1012	1.6238	1.2005	3.7422	0.6012	1.61	1.5987	2.6258	2.5377
ax	0.8858	0.5111	0.927	2.8326	1.7957	1.668	3.3896	1.7249	2.2959	2.5866	2.6145	2.1766
mean	0.6605	0.511767	0.857167	2.9591	2.0923	2.111933	3.093733	1.5115	5.0284	2.2988	2.519667	2.7504
std	0.168166	0.075282	0.072044	0.110209	0.54554	0.977208	0.683084	0.673264	4.358348	0.497648	0.14218	0.575346
	Volunteer 7			**Volunteer 8**			**Volunteer 9**					
	TF 0.6	**TF 0.65**	**TF 0.7**	**TF 0.6**	**TF 0.65**	**TF 0.7**	**TF 0.6**	**TF 0.65**	**TF 0.7**			
sag	6.9625	2.6762	2.9765	4.635	2.0785	2.4454	3.5787	2.8598	5.2899			
cor	4.3822	1.2585	1.2329	1.7211	2.4217	1.6099	2.3852	5.5698	5.1958			
ax	3.9004	1.3951	2.7078	3.2203	0.8903	1.8459	1.9582	7.3657	2.8078			
mean	5.0817	1.7766	2.305733	3.192133	1.796833	1.967067	2.6407	5.2651	4.431167			
std	1.344393	0.638553	0.766498	1.189761	0.65615	0.351687	0.685792	1.852101	1.148536			

Direct Quality Measure Result Scaling Factors

Metric Name	**Scaling Factor**
MSE - Mean Squared Error	10^{-3}
RMSE - Root Mean Squared Error	10^{-2}
Direct pSNR - Peak Signal-to-Noise Ratio	10^{-2}
UQI - Universal Quality Index	1
SSIM - Structural Similarity Index	1
ERGAS - Erreur Relative Globale Adimensionnelle de Synthèse	10^{-4}
SCC - Spetail Correlation Coeffecient	1
SAM - Spectral Angle Mapper	1
RASE - Relative Average Spectral Error	10^{-3}
VIFP - Visual Information Fidelity	1

8 Appendix B - Ethics Approval

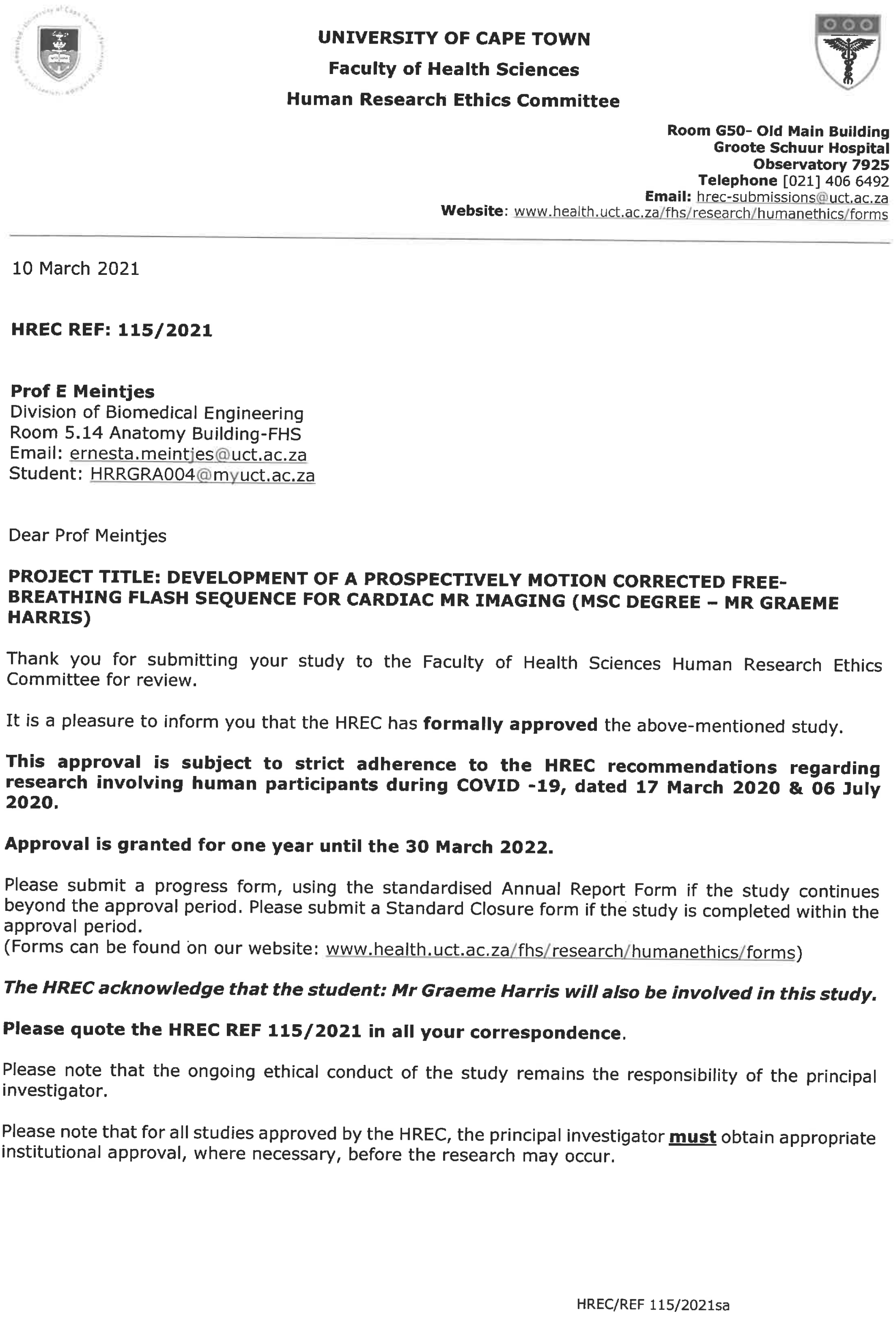

UNIVERSITY OF CAPE TOWN
Faculty of Health Sciences
Human Research Ethics Committee

Room G50- Old Main Building
Groote Schuur Hospital
Observatory 7925
Telephone [021] 406 6492
Email: hrec-submissions@uct.ac.za
Website: www.health.uct.ac.za/fhs/research/humanethics/forms

---

10 March 2021

HREC REF: 115/2021

Prof E Meintjes
Division of Biomedical Engineering
Room 5.14 Anatomy Building-FHS
Email: ernesta.meintjes@uct.ac.za
Student: HRRGRA004@myuct.ac.za

Dear Prof Meintjes

PROJECT TITLE: DEVELOPMENT OF A PROSPECTIVELY MOTION CORRECTED FREE-BREATHING FLASH SEQUENCE FOR CARDIAC MR IMAGING (MSC DEGREE – MR GRAEME HARRIS)

Thank you for submitting your study to the Faculty of Health Sciences Human Research Ethics Committee for review.

It is a pleasure to inform you that the HREC has **formally approved** the above-mentioned study.

This approval is subject to strict adherence to the HREC recommendations regarding research involving human participants during COVID -19, dated 17 March 2020 & 06 July 2020.

Approval is granted for one year until the 30 March 2022.

Please submit a progress form, using the standardised Annual Report Form if the study continues beyond the approval period. Please submit a Standard Closure form if the study is completed within the approval period.
(Forms can be found on our website: www.health.uct.ac.za/fhs/research/humanethics/forms)

The HREC acknowledge that the student: Mr Graeme Harris will also be involved in this study.

Please quote the HREC REF 115/2021 in all your correspondence.

Please note that the ongoing ethical conduct of the study remains the responsibility of the principal investigator.

Please note that for all studies approved by the HREC, the principal investigator **must** obtain appropriate institutional approval, where necessary, before the research may occur.

Yours sincerely

Signed by candidate

PROFESSOR M BLOCKMAN
CHAIRPERSON, FACULTY OF HEALTH SCIENCES HUMAN RESEARCH ETHICS COMMITTEE
Federal Wide Assurance Number: FWA00001637.
Institutional Review Board (IRB) number: IRB00001938
NHREC-registration number: REC-210208-007

This serves to confirm that the University of Cape Town Human Research Ethics Committee complies to the Ethics Standards for Clinical Research with a new drug in patients, based on the Medical Research Council (MRC-SA), Food and Drug Administration (FDA-USA), International Council for Harmonisation of Technical Requirements for Pharmaceuticals for Human Use: Good Clinical Practice (ICH GCP), South African Good Clinical Practice Guidelines (DoH 2006), based on the Association of the British Pharmaceutical Industry Guidelines (ABPI), and Declaration of Helsinki (2013) guidelines. The Human Research Ethics Committee granting this approval is in compliance with the ICH Harmonised Tripartite Guidelines E6: Note for Guidance on Good Clinical Practice (CPMP/ICH/135/95) and FDA Code Federal Regulation Part 50, 56 and 312.